Ore Geology Reviews 84 (2017) 42–66

Contents lists available at ScienceDirect

Ore Geology Reviews

journal homepage: www.elsevier.com/locate/oregeorev

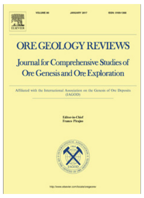

Geology, mineralogy and evolution of iron skarn deposits in the Zanjan district, NW Iran: Constraints from U-Pb dating, Hf and O isotope analyses of zircons and stable isotope geochemistry

Ghasem Nabatian [a,*], Xian-Hua Li [b], Maryam Honarmand [c], Joan Carles Melgarejo [d]

[a] Department of Geology, Faculty of Sciences, University of Zanjan, Zanjan 45195-313, Iran
[b] State Key Laboratory of Lithospheric Evolution, Institute of Geology and Geophysics, Chinese Academy of Sciences, Beijing 100029, China
[c] Department of Earth Sciences, Institute for Advanced Studies in Basic Sciences (IASBS), PO Box 45195-1159, Zanjan, Iran
[d] Departament de Mineralogia, Petrologia i Geologia Aplicada, Universitat de Barcelona, c/Martí i Franquès s/n, 08028 Barcelona, Catalonia, Spain

ARTICLE INFO

Article history:
Received 26 December 2015
Received in revised form 12 October 2016
Accepted 22 October 2016
Available online 1 November 2016

Keywords:
Magnesian and calcic iron skarn
U–Pb zircon dating
Hf and O isotopes
Eocene magmatism
Zanjan

ABSTRACT

The Zanjan iron skarn deposits are located in the northwest Central Iranian terrane, along the Soltaniyeh mountains. The deposits are hosted by late Proterozoic to late Cambrian carbonate rocks (Soltaniyeh, and Mila Formations) and by Permian (Ruteh Formations), intruded by the Arjin granite, the Khakriz granodiorite and the Inche-Rahbari quartzmonzonite (53 ± 1 Ma to 55 ± 0.4 Ma, early Eocene). These granitoids show high-K calc-alkaline, metaluminous affinity and have similar geochemical features, including strong enrichment of LILEs and LREEs, and depletion in high field strength elements (HFSEs) and HREE. The Arjin, Khakriz and Inche-Rahbari granitoid samples show zircon $\varepsilon\mathrm{Hf}_{(t)}$ values of −0.7 to +5.8 (T_{DM2} = 1052–1640 Ma) and $\delta^{18}O$ values of +5.55‰ to +7.42‰ suggesting partial melting of older crustal material then mixing with juvenile mantle-derived melts. The thermal anomaly induced by underplating mafic melts resulted in partial melting of continental crust and formation of Arjin, Khakriz and Inche-Rahbari magmas emplaced during several magmatic pulses at 53–55 Ma.

The Zanjan iron skarn deposits are magnesian (Arjin and Inche-Rahbari) and calcic (Khakriz) with endoskarn and exoskarn facies. In these skarn facies forsterite, garnet and pyroxene comprise the main prograde skarn minerals, whereas magnetite, serpentine, amphiboles of the tremolite-ferroactinolite series (sometimes asbestiform), epidote, talc and calcite are the principal retrograde skarn minerals. Iron exoskarns formed at the contacts of the intrusions parallel to the fabric of the host rocks and in networks of crosscutting veins and veinlets. The assemblage of ore minerals consists of magnetite, hematite (specularite), pyrite, chalcopyrite and bornite; in addition, minor galena and sphalerite occur in the Khakriz deposit. The sulfur isotopic compositions in the Arjin deposit range from +15.99 to +18.35‰ and in the Inche-Rahbari and Khakriz deposits from +2.96 to 5.30‰. The oxygen and carbon isotope ratios of the fresh or partly altered limestones from Soltaniyeh and Mila Formations reveal $\delta^{13}C$ values of −0.64 to +0.03‰ and $\delta^{18}O$ composition of +13.12 to +24.41‰ typical of marine carbonate. The isotopic compositions of the hydrothermal calcite (skarn calcite) range from −5.32 to −2.01‰ for carbon isotope and 3.29 to 20.67‰ for oxygen isotope. Complex water-rock interaction between the ore-bearing magmatic fluids and sedimentary wall rocks was responsible for sulfur, oxygen and carbon mixing. Field observations, mineral paragenesis, and stable isotopic signatures in these deposits are consistent with ore mineralization formed by the interaction of magmatic fluids with both cooler meteoric water and carbonate host rocks.

© 2016 Elsevier B.V. All rights reserved.

1. Introduction

Skarn deposits are one of the more abundant ore types in the Earth's crust and form in rocks of all ages (Einaudi et al., 1981; Meinert et al., 2005). This type of deposit has been mined for Fe, Cu, Pb, Zn, W, Sn, Mo, Au, Ag, U, REE, F and B (Mueller, 1991; Mueller et al., 1991; Meinert, 1983, 1992; Jamtveit and Andersen, 1993; Romer and Soler, 1995; Kunzmann, 1999; Forster et al., 2004; Ganino et al., 2008). Skarn type deposits are epigenetic and form as a result of contact-metamorphism and a variety of metasomatic processes involving magmatic, metamorphic and meteoric fluids (Pan and Dong, 1999;

---

* Corresponding author.
E-mail address: gh.nabatian@znu.ac.ir (G. Nabatian).

http://dx.doi.org/10.1016/j.oregeorev.2016.10.029
0169-1368/© 2016 Elsevier B.V. All rights reserved.

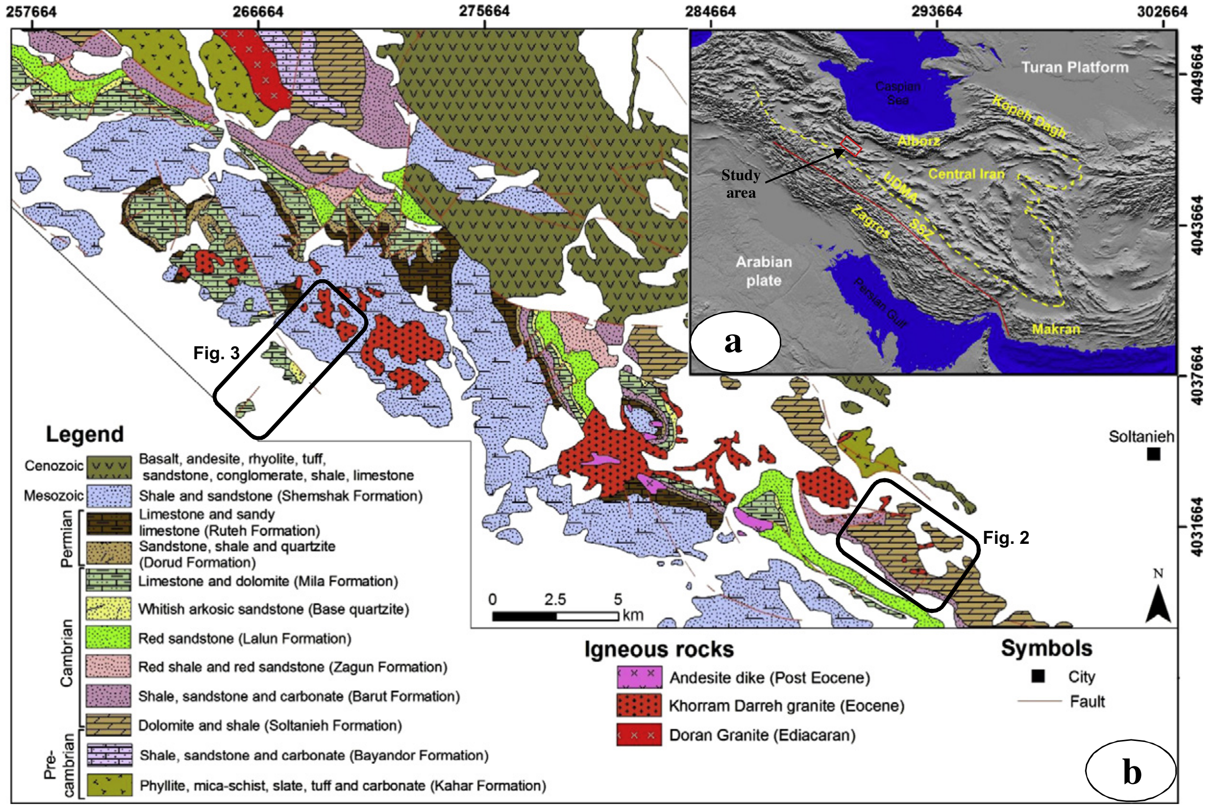

Fig. 1. (a) Simplified structural map of Iran and adjacent regions. Inset shows the location of the study area in the Central Iran structural zone; (b) Simplified geological map of the Zanjan district (after Stocklin and Eftekharnezhad, 1969). Small rectangles show the location of Figs. 2 and 3. We used UTM system for this figure.

O'Neill et al., 2002; Meinert et al., 2005; Chen et al., 2007; Pirajno, 2009; Wan et al., 2010). According to Einaudi et al. (1981) and Meinert et al. (2000), Fe skarns are the largest skarn deposits. Iron skarn type deposits may have minor amounts of Cu, Co, Au and Ni (Pirajno, 2009).

Iron deposits in Iran were formed during several metallogenic phases, the most important phases during the Neoproterozoic to early Cambrian (Kiruna-type deposits) and Cenozoic (skarn deposits) (Karimpour, 1989; Foster and Jafarzadeh, 1994; Mazaheri et al., 1994; Daliran, 2002; Maanijou, 2002; Daliran et al., 2007, 2010; Jami et al., 2007; Golmohammadi et al., 2014; Nabatian et al., 2015). The deposits are mainly located in the Alborz magmatic zone (Alborz), Urumieh-Dokhtar magmatic arc (UDMA), Sanandaj-Sirjan magmatic-metamorphic zone (SSZ) and Central Iranian Zone (CIZ). Most of the iron skarn deposits in the UDMA, Alborz and CIZ are related to Cenozoic magmatism which occurred during the subduction and closure of the Neo-Tethys Ocean. The most important Fe skarn deposits in the Alborz are the Semnan deposits and Fe-Cu skarn deposits in the Azarbaijan district (Karimzadeh Somarin and Moayyed, 2002). The Niyasar iron deposits in the Kashan region, Daran deposit in the Esfahan area, Arjin, Khakriz and Inche-Rahbari deposits in the Zanjan district, Panjkuh and Sangan deposits are the main skarn type iron deposits in the UDMA and CIZ. The Arjin, Khakriz and Inche-Rahbari iron skarn deposits in the Zanjan district are located in the Soltaniyeh-Mahabad metallogenic axis. This metallogenic axis mainly contains iron mineralization which is hosted by Precambrian to late Paleozoic sequences (Nabatian et al., 2015 and references therein).

We present new field observations, whole rock geochemistry, U-Pb zircon ages, oxygen and Lu-Hf isotopic compositions of zircon and stable isotope data to better understand the age and origin of the magmatic rocks and the evolution of Fe skarns in the Zanjan district, Northwest of Iran. This is the first detailed study of plutonism and iron mineralization in this region. Our results have important implications for understanding the geodynamic framework of Eocene magmatism in the Central Iranian zone, and for the formation of iron skarn deposits.

2. Geological setting

The Zagros part of the Alpine-Himalayan orogenic belt in Iran resulted from the closure of the Neotethyan Ocean between the African-Arabian and Eurasian plates (Berberian and King, 1981; Sengör et al., 1988; Alavi, 1994, 2007; Agard et al., 2005). This orogen extends from eastern Turkey (Bitlis suture zone) through northern Iraq and SW Iran into northern Oman, and contains three parallel tectonic zones: the UDMA, SSZ and the Zagros fold-and-thrust belt (Alavi, 2004).

The Neo-Tethys Ocean was eliminated by the collision of the Arabian-Eurasian plates during the Late Cretaceous to the Miocene (Berberian and King, 1981; Berberian and Berberian, 1981; Alavi, 1994; Mohajjel and Fergusson, 2000; Vincent et al., 2005; Agard et al., 2005, 2011; Horton et al., 2008; Ballato et al., 2011; Verdel et al., 2011). During this time, subduction of oceanic crust caused widespread magmatic activity throughout the Iranian plateau especially in the CIZ, Alborz, UDMA and Eastern Iran (Agard et al., 2005, 2011; Verdel et al., 2011; Chiu et al., 2013; Asiabanha and Foden, 2012; Honarmand et al., 2014; Nabatian et al., 2014). This magmatic activity was responsible for different mineralization styles such as porphyry Cu-Mo, epithermal Au-Pb-Zn, Kiruna-type iron deposits, orogenic gold and skarn type iron deposits in the Iranian plateau.

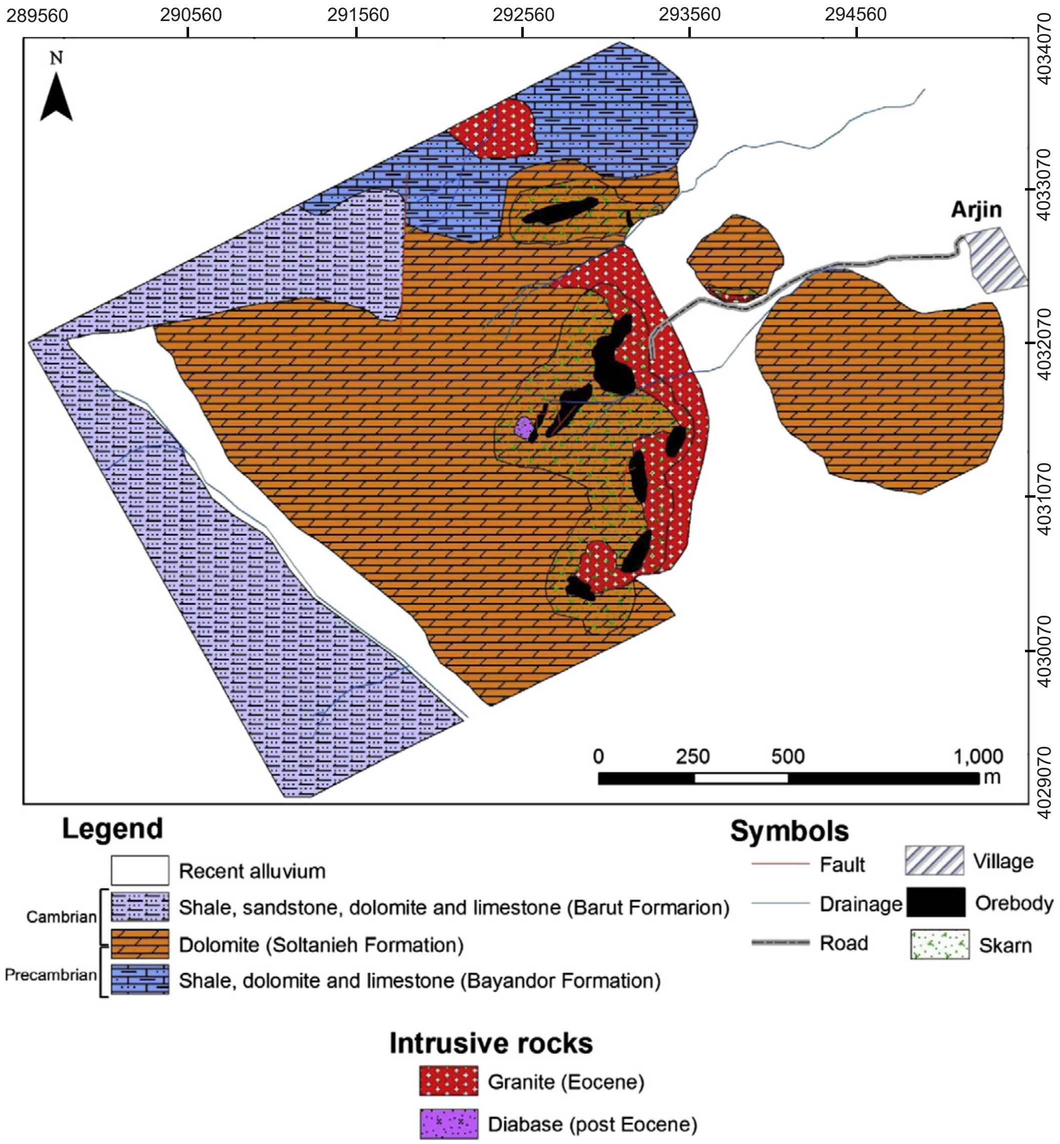

Fig. 2. Geological map of the Arjin deposit. We used UTM system for this figure.

The study area is located in the northwest CIZ (Fig. 1), in the hinterland of the Zagros orogeny and is flanked by the Alborz Mountains in the north and the SSZ to the south (Fig. 1). The Zanjan district consists of a large crustal block made up of metamorphic rocks, granitic intrusions and late Proterozoic-Cambrian to Cenozoic sedimentary strata. The oldest rock units consist of the Kahar, Bayandor, Soltanieh, Barut, Zaigun, Lalun, Mila, Doroud and Ruteh Formations. Among them, the Soltanieh, Mila and Ruteh formations host the iron skarn mineralization in the Zanjan district (Figs. 1, 2 and 3).

The Soltanieh Formation consists of five lithostratigraphic units, a) Lower Dolomite Member, b) Lower Shale Member (or Chopoghloo Member), c) Middle Dolomite Member, d) Upper Shale Member, and e) Upper Dolomite Member. Based on the fossil content, the ages of both a and b members belong to the late Proterozoic whereas c, d and e members belong to the lower Cambrian (Jafari et al., 2007). The Soltanieh Formation of the Alborz Mountains and Central Iran contains sedimentary phosphate deposits within the lower horizons.

The Mila Formation of Cambrian-Ordovician age consists of carbonates (dolomite and limestone) and shales with white quartzites at the base. According to Stocklin et al. (1964) the Mila Formation comprises five members, a) Basal quartzites (white quartzites) with dolomitic cement, b and c) Dolostones and cherty dolostones, oolithic limestones and subordinate marls, d) Cherty limestones, limestones and sandstones, e) Limestones, greenish grey shales and dolomitic limestone. In the Zanjan area, the Mila Formation is unconformably overlain by red sandstones, quartzites and shales of the Doroud Formation of Permian age. The Doroud Formation is covered by the limestones of Ruteh Formation. Rocks of the Doroud and Ruteh Formations are dominant in the outcrops of the Khakriz area (Fig. 3). The Jurassic Shemshak Formation is largely exposed in the Southern part of the district and consists of shales and sandstones (Fig. 1b). Magmatism in the study area commenced with the emplacement of granitic intrusions of the Khakriz, Inche-Rahbari and Arjin (KIAG) suite, followed by andesitic dikes.

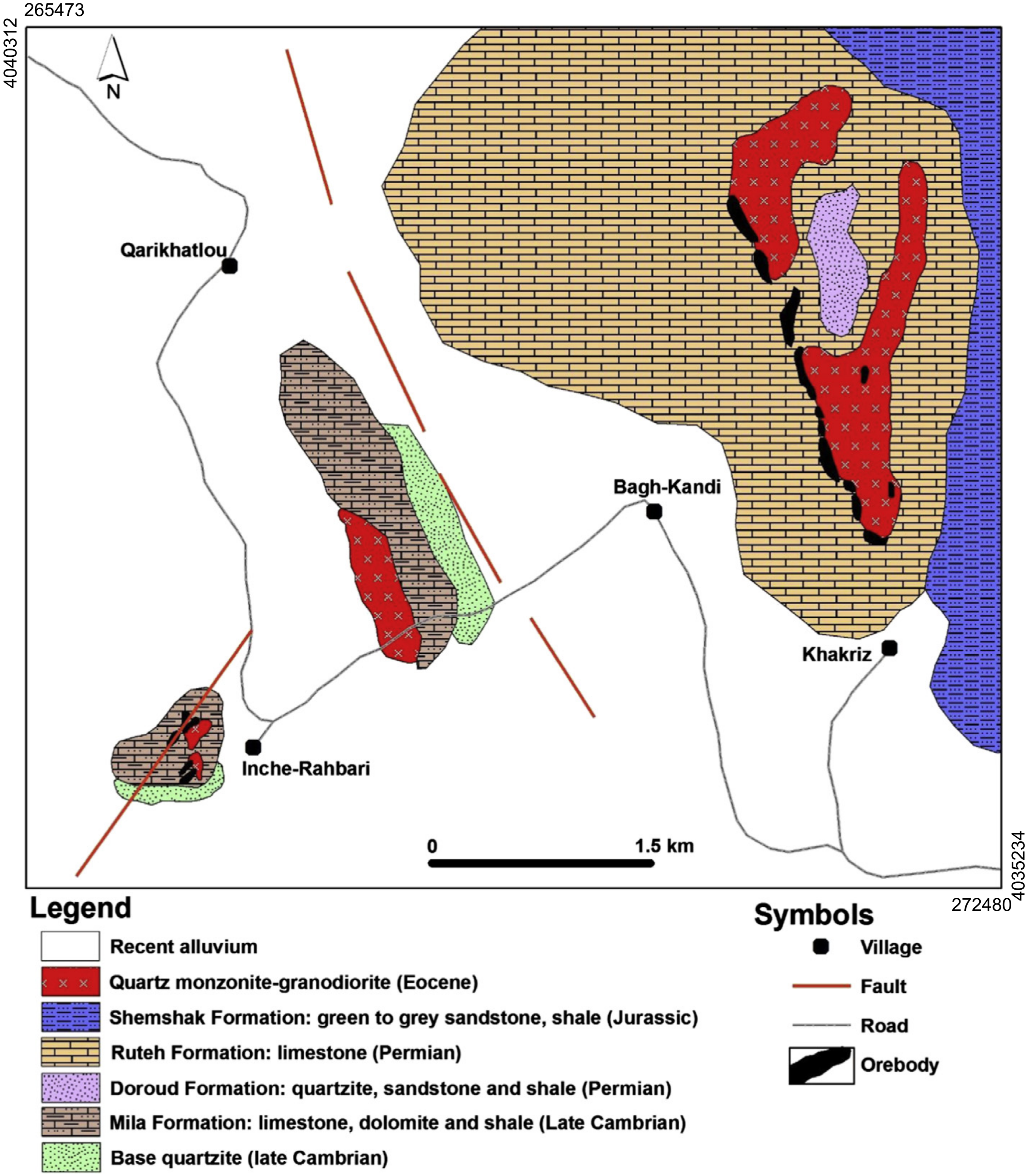

Fig. 3. Geological map of the Khakriz and Inche-Rahbari deposits. We used UTM system for this figure.

3. Analytical methods

3.1. Whole rock geochemistry

Whole-rock chemical analyses were performed for a total of 9 samples from the Arjin, Khakriz and Inche-Rahbari intrusions. Major elements were determined at the Zarazma Laboratory, Iran by inductively coupled plasma optical emission spectrometry (ICP-OES) following a lithium metaborate fusion and dissolution by nitric acid. Trace elements and rare-earth elements were measured at West Lab (Australia) by inductively coupled plasma mass spectrometry (ICP-MS) following 4-acid digestion.

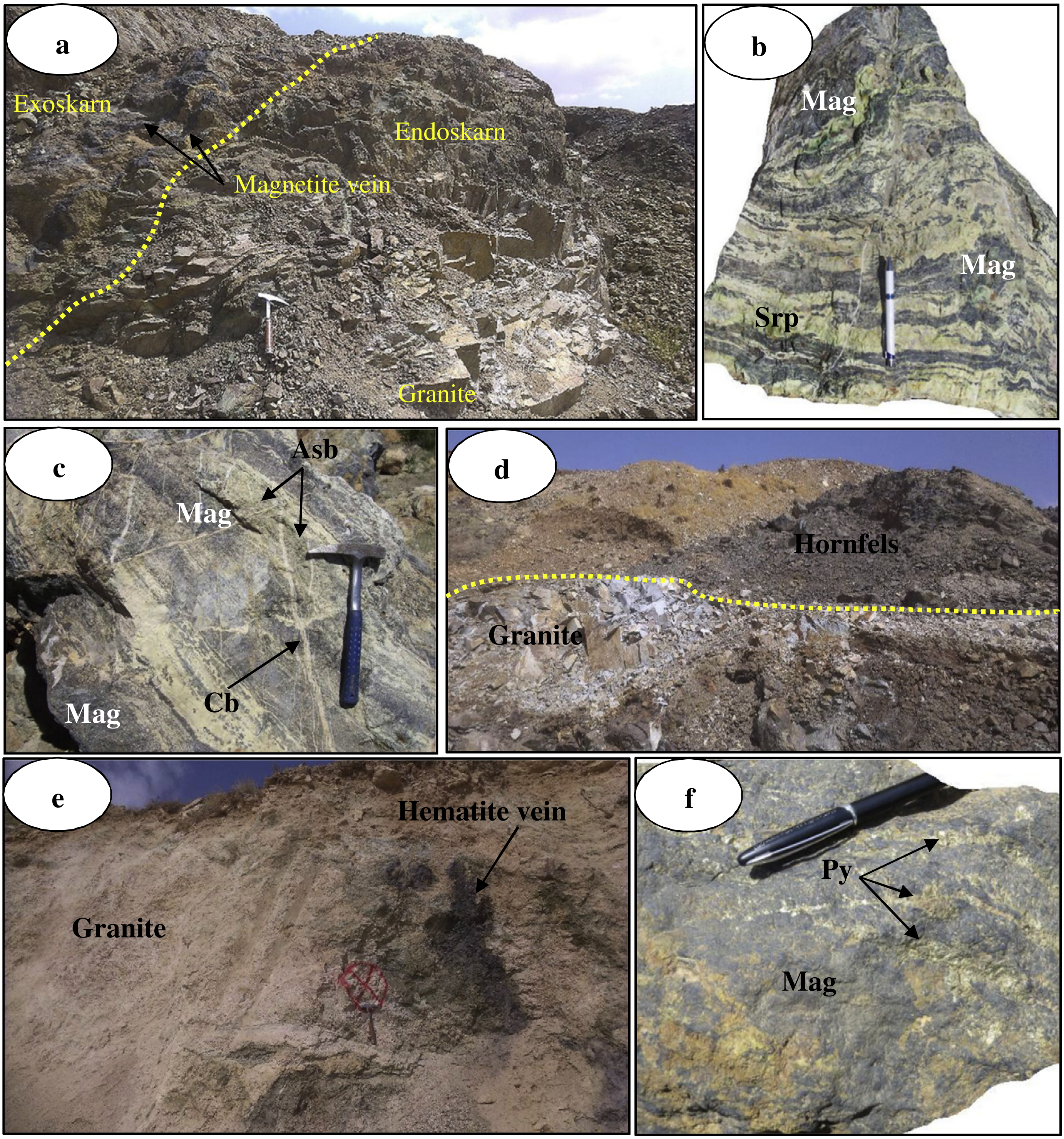

Fig. 4. Photographs of skarn and hornfels in the Khakriz and Arjin deposits. (a) Field photograph showing the spatial association of the granitic pluton with iron skarn in the Khakriz deposit; (b), (c) Banded iron skarn from the Arjin deposit. The prograde skarn consists of alternating garnet (grossular-andradite) and retrograde magnetite (Mag) bands, serpentine (Srp) and asbestos (Asb) crosscut by late-stage carbonate (Cb) veins; (d) Pyroxene hornfels facies is developed within a restricted zone close to the contact with the Khakriz pluton; (e) Hematite mineralization within the granite of the Arjin deposit; (f) pyrite (Py) veins cross-cutting the magnetite (Mag) orebody of the Khakriz deposit.

3.2. Zircon U-Pb dating

Zircon crystals were separated from rock samples of 1-kg each using standard density and magnetic techniques. Zircon grains, together with zircon standards (Plěsovice, Qinghu and Penglai) were mounted in epoxy mounts which were then polished for analysis. All zircons were documented using transmitted and reflected light micrographs as well as cathodoluminescence (CL) images to study their internal structures and find a suitable point for analysis. The mount was vacuum-coated with high-purity gold. Measurements of U, Th and Pb isotopes were

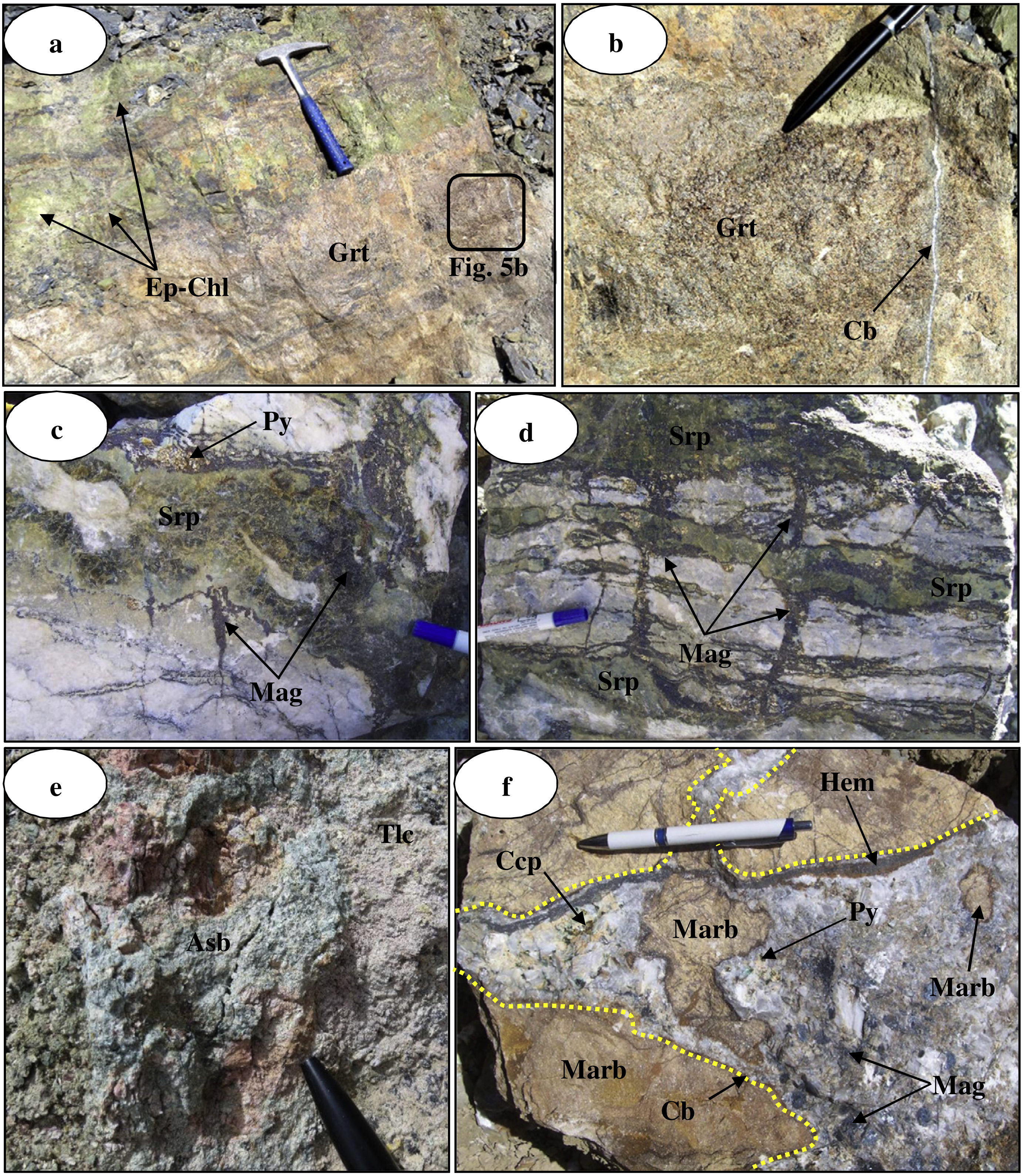

Fig. 5. Photographs of prograde and retrograde skarn, Khakriz and Arjin deposits. (a), (b) Calcic skarn composed of garnet (Grt) and retrograde epidote + chlorite (Ep + Chl), Khakriz deposit. The inset rectangle outlines Fig. 5b; (c), (d) Magnesian skarn, Arjin deposit, retrograde serpentine (Srp) formed around the magnetite veins; (e) asbestos (Asb) and talc (Tlc) in the Arjin deposit; (f) Late-stage carbonate breccia vein (Cb) with a hematite margin (Hem) crosscutting marble in the Arjin deposit. The vein contains fragments of marble (Marb), magnetite (Mag), pyrite (Py), and chalcopyrite (Ccp).

conducted using a Cameca IMS 1280 large-radius SIMS at the Institute of Geology and Geophysics, Chinese Academy of Sciences (IGG-CAS) in Beijing.

Data processing procedures are similar to those described by Li et al. (2009a). U-Th-Pb isotope ratios were calibrated relative to the Plěsovice zircon standard (^{206}Pb/^{238}U = 0.05369, 337.1 Ma;

Sláma et al., 2008), and absolute element abundances were determined relative to the M257 zircon standard (U = 840 ppm, Th/U = 0.27; Nasdala et al., 2008). A long-term uncertainty of 1.5% (1 sigma) for ^{206}Pb/^{238}U measurements of the standard zircons was applied to the unknowns (Li et al., 2010a), even though the measured ^{206}Pb/^{238}U error during the course of this study is ca. 1% (1 sigma). The ^{204}Pb-method was used for the common lead correction. An average Pb of present-day crustal composition (Stacey and Kramers, 1975) was used as common lead assuming surface contamination introduced during sample preparation. Uncertainties on individual analyses in the data tables are reported at a 1σ level; mean ages for pooled U/Pb analyses are quoted with 95% confidence. Data reduction was carried out using the Isoplot/Ex v. 2.49 program (Ludwig, 2003).

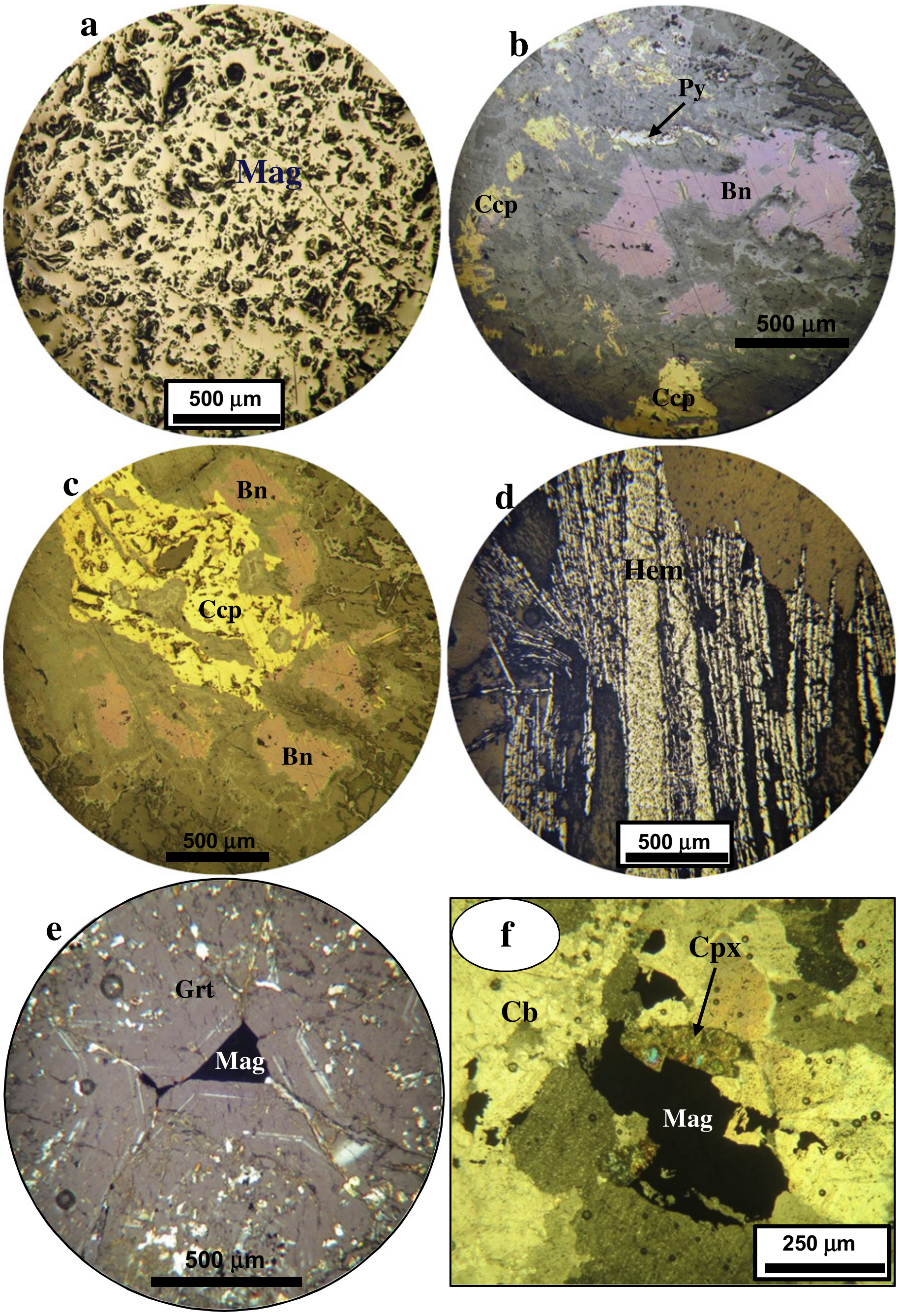

Fig. 6. Photomicrographs of ore minerals and skarn minerals. (a) retrograde massive magnetite (Mag) ore (reflected light; ppl); (b, c) intergrowth of retrograde chalcopyrite (Ccp), pyrite (Py) and bornite (Bn) (reflected light; ppl); (d) retrograde late-stage hematite (Hem); (e) prograde garnet (Grt) and retrograde magnetite (Mag) (reflected light; ppl); (f) retrograde magnetite (Mag) replacing clinopyroxene (Cpx) within the carbonate (Cb) host rock (exoskarn) in the Inche-Rahbari deposit (transmitted light; xpl); (g) retrograde serpentine (Srp) crosscut by a late-stage carbonate (Cb) vein (transmitted light; xpl); (h) retrograde asbestos (Asb) and talc (Tlc) in the Inche-Rahbari deposit (transmitted light; xpl); (i, j) retrograde tremolite-actinolite (Tr) and epidote (Ep) within the Khakriz intrusion (transmitted light; xpl).

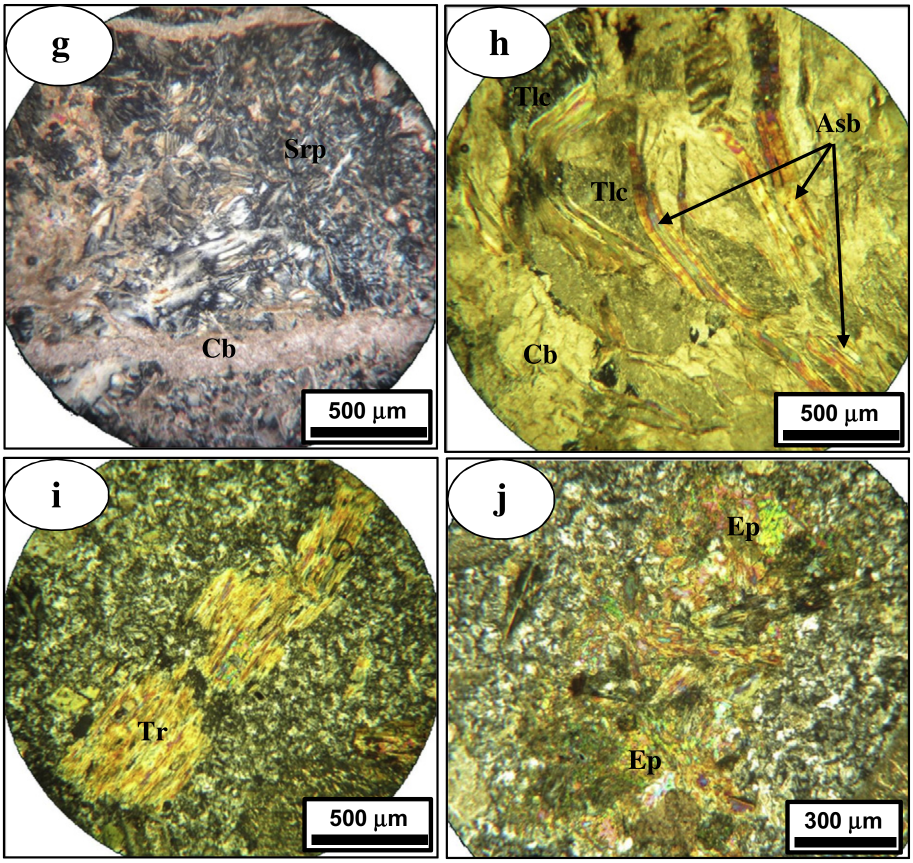

3.3. Zircon oxygen isotopes

Zircon oxygen isotopes were measured using the same Cameca IMS 1280 SIMS. The Cs^+ primary ion beam was accelerated at 10 kV, with an intensity of 2 nA (Gaussian mode with a primary beam aperture of 200 µm to reduce aberrations) and rastered over a 10 µm area. The spot was about 30 µm in diameter. Isotopes ^{16}O and ^{18}O were collected simultaneously using two Faraday cups, and the mass resolution used was 2500 during the analyses. The instrumental mass fractionation factor (IMF) was corrected using the Penglai zircon standard ($\delta^{18}O = 5.3‰$, Li et al., 2010b); the Qinghu zircon standard was used for quality control (QC). The measured $^{18}O/^{16}O$ ratios were normalized by using Vienna Standard Mean Ocean Water compositions (VSMOW, $^{18}O/^{16}O = 0.0020052$). A second Qinghu zircon standard ($\delta^{18}O = 5.5‰$) was analyzed as an unknown to ascertain the veracity of the IMF. $\delta^{18}O$ measurements of Qinghu zircon during the course of this study yield a weighted mean of $\delta^{18}O = 5.54 \pm 0.42‰$ (2σ), which is within error of the reported value of $5.5 \pm 0.2‰$ (Li et al., 2013). Uncertainties on individual analyses are reported at the 2σ level. Detailed analytical techniques and data processing procedures were similar to those described by Li et al. (2009b) and Tang et al. (2015).

3.4. Zircon Lu-Hf isotopes

In situ zircon Lu-Hf isotopic analyses were performed on a Neptune multi-collector LA-ICP-MS at the IGG-CAS. Lu-Hf isotopic analyses were obtained on the same point of zircon grains that were previously analyzed for U-Pb and O isotopes, with ablation pits of 60 µm (44 µm for grains small) in diameter, ablation time of 26 s, repetition rate of 8 Hz (6 Hz for ablation pits of 44 µm), and laser beam energy density of 10 J/cm^2. The detailed analytical procedures were similar to those described by Wu et al. (2006). Measured $^{176}Hf/^{177}Hf$ ratios were normalized to $^{179}Hf/^{177}Hf = 0.7325$. The $^{176}Hf/^{177}Hf$ ratios for zircon standards MUD (0.2825226 ± 0.0000029) and GJ1 (0.2820281 ± 0.0000045) are in good agreement with the reported values (Griffin et al., 2006; Wu et al., 2006).

3.5. Stable isotopes (S, O and C)

Sulfur isotope analyses were carried out at the University of Barcelona on 19 single sulfide grains from the three studied deposits: 10 samples from Arjin, 5 from Khakriz and 4 from Inche-Rahbari. Isotopic analyses were done in a Finnigan CHN Elemental Analyser, where sulphide samples are burned and the sulphur of the samples is transformed into SO_2. The Elemental Analyser is coupled to an isotope ratio mass spectrometer Thermo Delta Plus XP, in which the produced SO_2 is analysed. The $\delta^{34}S$ ratios were calibrated using the IAEA S1, IAEA S2, IAEA S3 and NBS-123 international standards. The 2-sygma analytical error was less than 1.0‰ of the isotope ratio. A total of 19 carbonate samples were selected in order to analyze their $^{13}C/^{12}C$ ratios. 50 µg of each sample were taken using a drill. CO_2 extraction was done in a Thermo Finnigan Carbonate Kiel Device III, which reproduces in an automated way a modified version of the McCrea method (McCrea, 1950). Carbonate is attacked with 100% phosphoric acid at a 70 °C, with a 5 min reaction time. The Carbonate Device is coupled to an isotope ratio mass spectrometer Thermo Finnigan

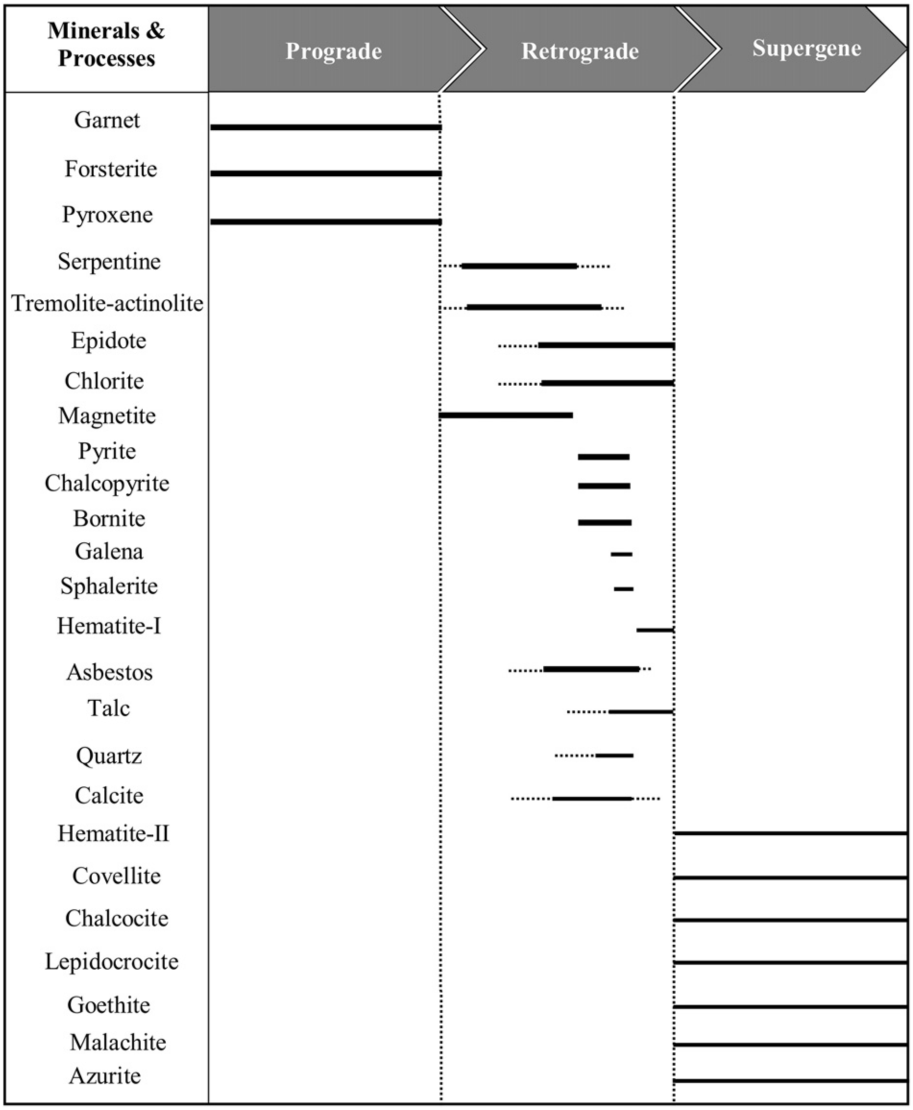

Fig. 7. Paragenetic sequence of mineralization in the Arjin, Inche-Rahbari and Khakriz deposits. The Mg-bearing minerals such as forsterite, serpentine, asbestos and talc occur in the Arjin and Inche-Rahbari deposits and sphalerite and galena in the Khakriz deposit.

MAT-252, where the produced CO_2 is analysed. Results were calibrated with the NBS-18 and NBS-19 international standards. The 2-sygma analytical error was less than 0.04‰ for $\delta^{13}C$ and 0.12‰ for $\delta^{18}O$.

4. Eocene intrusive rocks

The KIAG intrusions are located in the central portion of the Soltanieh Mountains west of Soltanieh city (Fig. 1b). The composition of the plutons varies from granodiorite to biotite granite with seriate or porphyritic texture. The Khakriz (granodiorite) and Inche-Rahbari (quartz monzonite to monzogranite) samples consist of plagioclase, quartz, orthoclase and minor clinopyroxene ranging in size from 0.5 to 2 mm set in a fine-grained groundmass dominated by feldspar and amphibole (hornblende). Plagioclase phenocrysts typically occur as subhedral to rarely anhedral crystals with compositional zoning and albite twinning, whereas K-feldspar forms euhedral to subhedral crystals with Karlsbad twinning. The Khakriz granodiorite contains more phenocrysts than the Inche-Rahbari granite. Accessory minerals are biotite, hornblende and minor amounts of titanite, apatite, zircon and magnetite.

The Arjin granite is composed of quartz, orthoclase and minor plagioclase together with biotite as the main ferromagnesian mineral. Orthoclase typically occurs as subhedral to rarely anhedral crystals (up to 1.5 mm) and is altered to clay minerals. Biotite forms subhedral crystals with inclusions of magnetite and zircon. In some cases, it is replaced by secondary minerals such as chlorite and iron oxides. Quartz is anhedral. Granophyric texture is well developed between quartz and K-feldspar. Hornblende, magnetite and apatite are the accessory minerals in the Arjin granite. In some cases, amphibole and biotite are replaced by chlorite and iron oxides.

The andesitic dikes show porphyritic texture with plagioclase and hornblende phenocrysts embedded in a fine grained groundmass made up by plagioclase and altered mafic minerals. The secondary minerals include epidote, chlorite, calcite and sericite.

Table 1
Major (wt%) and trace (ppm) element concentrations of the KIAG intrusions.

ID	Khakriz intrusion			Arjin intrusion			Inche-Rahbari intrusion		
	KH-2	KH-43	KH-47	AJ-30	AJ-33	AJ-34	IN-4	IN-51	IN-53
SiO_2	68.34	67.14	69.16	76.63	76.67	76.76	67.69	70.31	70.33
TiO_2	0.39	0.42	0.40	0.10	0.12	0.13	0.48	0.42	0.44
Al_2O_3	15.31	15.22	14.65	12.12	12.03	12.44	15.32	14.48	14.63
$FeO_{(t)}$	1.69	1.83	1.78	1.06	1.09	0.75	1.66	1.20	1.32
Fe_2O_3	1.88	2.04	1.98	1.18	1.21	0.83	1.85	1.33	1.47
MnO	0.05	0.05	0.05	0.05	0.05	0.05	0.05	0.05	0.05
MgO	1.20	1.25	1.30	0.15	0.40	0.13	1.63	1.22	1.48
CaO	2.64	3.25	3.30	0.39	0.41	0.27	2.30	2.27	2.20
Na_2O	4.72	4.54	4.03	3.50	3.71	3.25	5.64	5.00	6.16
K_2O	3.96	4.09	3.86	5.16	4.55	5.13	3.85	4.10	2.39
P_2O_5	0.11	0.16	0.11	0.05	0.05	0.05	0.18	0.14	0.16
LOI	1.20	1.65	0.93	0.58	0.70	0.86	0.83	0.50	0.58
Ag	0.14	0.14	0.14	0.73	0.40	0.15	0.32	0.25	0.45
As	1.40	2.40	1.70	2.50	3.20	2.20	3.50	6.20	4.10
Ba	1120	1090	1260	1397	1401	1532	962	1120	811
Be	2.50	2.60	2.80	4.40	5.50	2.50	2.90	3.00	2.40
Bi	0.10	0.20	0.30	0.20	0.50	0.10	0.30	0.30	0.20
Cd	<0.05	0.09	<0.05	<0.05	<0.05	<0.05	<0.05	<0.05	<0.05
Co	3.00	3.30	3.80	1.00	2.00	1.00	4.30	4.40	4.00
Cr	115.0	155.0	232.0	284.0	377.0	340.0	164.0	235.0	136.0
Cs	0.80	0.50	0.70	9.80	11.10	3.30	0.40	0.40	0.30
Cu	<0.2	1.30	1.10	54.40	69.70	4.40	2.90	3.30	35.30
Ga	17.70	19.00	18.30	15.10	14.70	13.80	20.70	20.30	19.80
Ge	0.86	0.86	0.85	1.33	1.30	1.08	0.84	0.81	0.64
Hf	1.32	2.57	1.92	1.54	1.21	1.03	2.37	2.01	1.62
In	0.03	0.02	0.03	<0.01	0.01	<0.01	0.02	0.02	0.03
Li	6.60	9.90	5.00	7.50	7.40	5.20	3.60	<0.5	1.30
Mn	342	413	385	53	55	66	215	139	117
Mo	0.30	0.40	0.60	0.60	0.60	0.80	0.40	1.50	0.40
Nb	16.10	17.40	18.50	18.70	21.00	19.30	21.50	21.50	19.10
Ni	14.00	13.00	16.00	5.00	7.00	9.00	22.00	24.00	28.00
P	642	734	555	55	66	82	855	643	857
Pb	7.60	13.70	11.50	17.10	14.70	10.60	7.10	9.40	3.20
Rb	79.80	74.90	64.10	343.00	361.00	272.00	71.30	77.70	61.80
Sb	0.90	1.50	0.80	0.70	0.80	0.50	0.90	1.60	0.90
Sc	4.00	3.00	3.00	<1	<1	1.00	4.00	4.00	5.00
Se	0.23	0.22	<0.05	0.09	<0.05	0.20	0.13	0.20	0.23
Sn	0.90	1.10	1.60	1.50	1.70	1.20	1.60	1.50	1.20
Sr	741	712	750	53	65	115	639	684	441
Ta	1.05	1.15	1.24	1.17	1.14	1.00	1.35	1.35	1.13
Te	<0.2	< 0.2	<0.2	<0.2	<0.2	<0.2	<0.2	<0.2	<0.2
Th	15.20	16.10	12.20	42.50	36.00	34.10	18.20	22.90	21.40
Ti	2140	2320	2270	544	600	638	2740	2470	2530
Tl	0.40	0.40	0.30	0.90	0.90	0.60	0.30	0.30	<0.1
U	4.23	4.23	5.58	5.34	5.98	2.03	3.40	4.24	2.81
V	33.0	37.0	36.0	6.0	7.0	7.0	41.0	37.0	37.0
W	0.80	0.90	1.20	2.50	2.90	1.40	0.60	0.70	0.40
Zn	24.80	31.20	31.00	7.60	9.50	5.60	21.00	14.40	19.80
Zr	35	87	64	45	37	33	80	60	44
Mg#	55.8	54.8	56.5	20.1	39.6	23.7	63.6	64.5	66.6
La	37	36	26	38	33	24	39	47	48
Ce	77.70	74.20	38.40	43.50	35.90	34.30	87.30	91.20	97.10
Pr	5.91	5.78	4.26	3.74	2.84	3.39	7.04	7.05	7.56
Nd	18.70	18.40	13.70	9.00	6.59	9.24	22.90	22.80	24.50
Sm	2.73	2.77	2.14	1.04	0.74	1.20	3.49	3.48	3.75
Eu	0.47	0.46	0.33	0.16	0.16	0.19	0.65	0.63	0.81
Gd	1.51	1.27	1.03	0.81	0.78	0.71	2.09	2.16	2.84
Tb	0.23	0.24	0.19	0.15	0.13	0.12	0.30	0.33	0.31
Dy	1.25	1.30	1.03	0.86	0.77	0.68	1.60	1.82	1.63
Ho	0.23	0.23	0.19	0.19	0.15	0.17	0.29	0.35	0.29
Er	0.61	0.66	0.55	0.55	0.38	0.44	0.81	1.00	0.80
Tm	0.07	0.08	0.07	0.09	0.06	0.07	0.10	0.13	0.10
Yb	0.52	0.63	0.51	0.82	0.58	0.59	0.69	0.94	0.67
Lu	0.06	0.08	0.07	0.13	0.09	0.08	0.09	0.12	0.08
Y	5.34	5.75	4.50	4.87	3.04	3.80	6.92	8.69	7.37

Detection limits (in ppm) for trace and rare earth elements are as following. Ag: 0.01; As: 0.5; Ba: 0.2; Be: 0.2; Bi: 0.1; Cd: 0.05; Co: 0.2; Cr: 2; Cs: 0.1; Cu: 0.2; Ga: 0.05; Ge: 0.05; Hf: 0.02; In: 0.01; Li: 0.5; Mn: 2; Mo: 0.1; Nb: 0.5; Ni: 2; P: 5; Pb: 0.2; Rb: 0.1; Sb: 0.1; Sc: 1; Se: 0.05; Sn: 0.2; Sr: 0.1; Ta: 0.01; Te: 0.2; Th: 0.02; Ti: 10; Tl:0.1; U: 0.02; V: 2; W: 0.1; Zn: 0.2; Zr: 1; La: 0.05; Ce: 0.05; Pr: 0.05; Nd: 0.02; Sm: 0.02; Eu: 0.02; Gd: 0.05; Tb: 0.02; Dy: 0.02; Ho: 0.02; Er: 0.05; Tm: 0.05; Yb: 0.05; Lu: 0.02; Y: 0.05.

5. Iron skarn deposits

Several skarn type iron deposits are present in the Zanjan district. They include Arjin, Shah Bolaghi, Bashkan, Ghovagh, Shahrak, Khakriz and Inche-Rahbari. The iron exoskarn of the Arjin deposit replaced the Soltanieh carbonate (Fig. 2); iron exoskarns of the Inche-Rahbari and the Khakriz deposits developed on the Mila and the Ruteh limestones, respectively (Fig. 3). The iron mineralization in these deposits consists

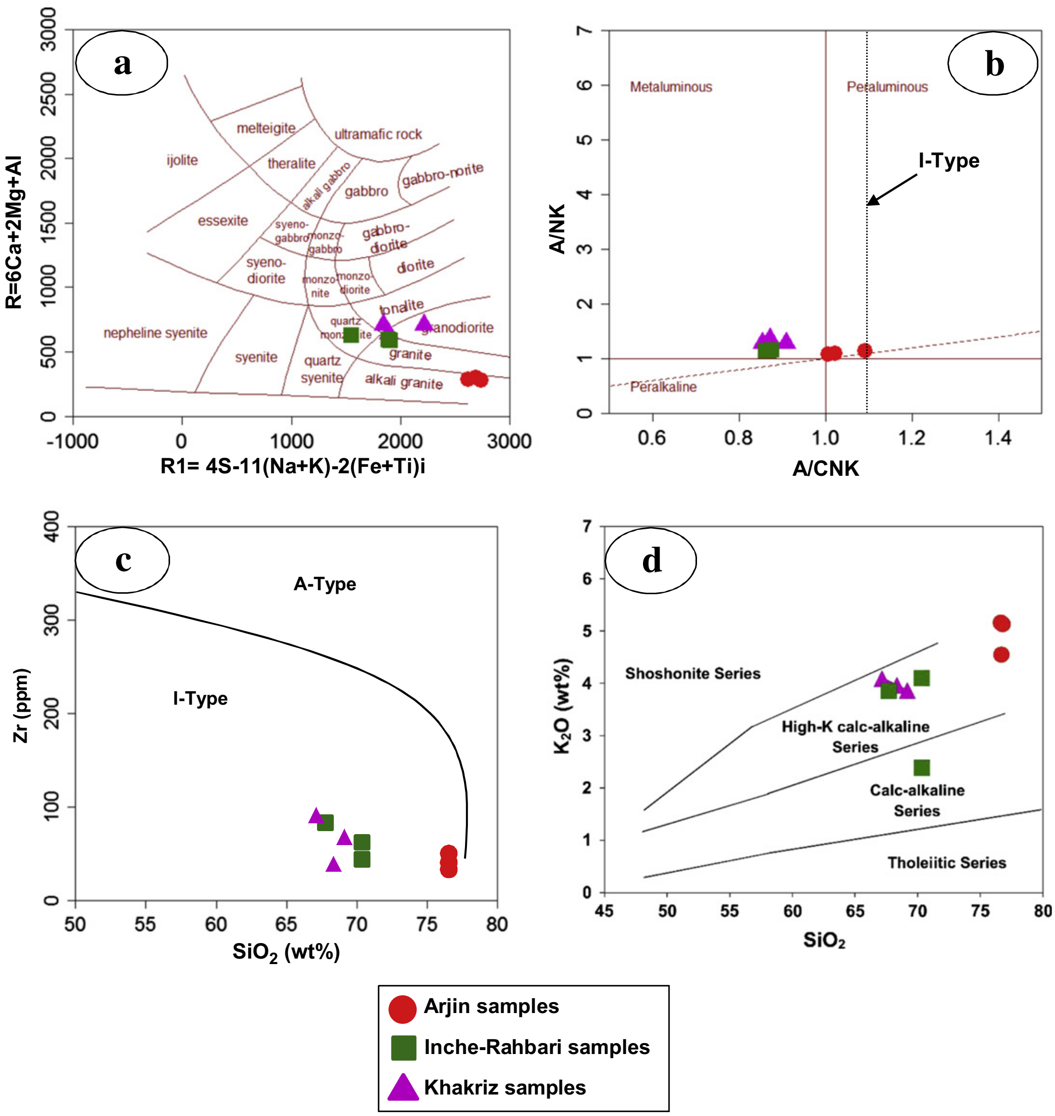

Fig. 8. Geochemical diagrams for the classification of the skarn-related KIAG intrusions, Zanjan district, Iran. (a) Granite classification diagram (De la Roche et al., 1980); (b) A/NK (molar) versus A/CNK diagram for granitic rocks of Maniar and Piccoli (1989). Dash line (A/CNK = 1.1) separates the I-type (A/CNK < 1.1) and S-type (A/CNK > 1.1) fields (from Chappell and White, 2001); (c) Zr vs. SiO_2 diagram Collins et al. (1982); (d) K_2O-SiO_2 diagram (Frost et al., 2001).

of stratabound, banded to massive bodies, veins and veinlets, breccias and disseminations of magnetite ± hematite with minor amounts of sulfides that are intergrown with calc-silicate minerals (Fig. 4). Moreover, the intrusion of the KIAG granites produced a thin metamorphic aureola (10 to 20 m thick) in the contact with the hosting shales, resulting in the development of hornfelses. These rocks can be easily identified in the field by a dictinct dark green to olive green color (Fig. 4d). These calc-silicate hornfelses formed due to the metasomatic reaction with the wall rock (shale) and are mainly composed of clinopyroxene. The hornfels facies are developed within a restricted zone close to the intrusive contact in the Khakriz, Inche-Rahbari and Arjin deposits.

The massive and vein orebodies (>50 wt% Fe) are confined to the contact of the skarns and the recrystallized carbonate rocks. The thickness of the orebodies varies from a few centimeters up to 30 m, and their length ranges from 50 to 100 m. The iron mineralization is mainly associated with exoskarns (Fig. 4a). In some cases, the KIAG intrusions are cut by veins and veinlets of magnetite and hematite in the vicinity of the contact.

Magnetite, hematite and sulfide minerals (e.g. pyrite and chalcopyrite) are the main ore minerals in the endoskarn. Clinopyroxene, chlorite, epidote and calcite with minor amounts of garnet are the characteristic metasomatic minerals in the endoskarn. Chlorite, epidote and calcite, as pseudomorphs of pyroxene, are the main retrograde minerals associated with opaque minerals in the endoskarn. The plagioclase is replaced by epidote and calcite and biotite is also replaced by chlorite.

The exoskarn in the Arjin and Inche-Rahbari deposits is composed chiefly of prograde minerals such as garnet, pyroxene and forsterite. These minerals are crosscut and replaced by the late stage ore and retrograde minerals.

The Khakriz skarn deposit is calcic and hosted by limestones of the Ruteh Formation, whereas the skarns in the Arjin and Inche-Rahbari deposits are magnesian. The gangue minerals comprise predominantly garnet, forsterite, diopside, serpentine, epidote, chlorite, asbestos minerals, talc, and calcite; magnetite, pyrite and chalcopyrite are the main ore minerals (Figs. 4f and 5). Magnesian

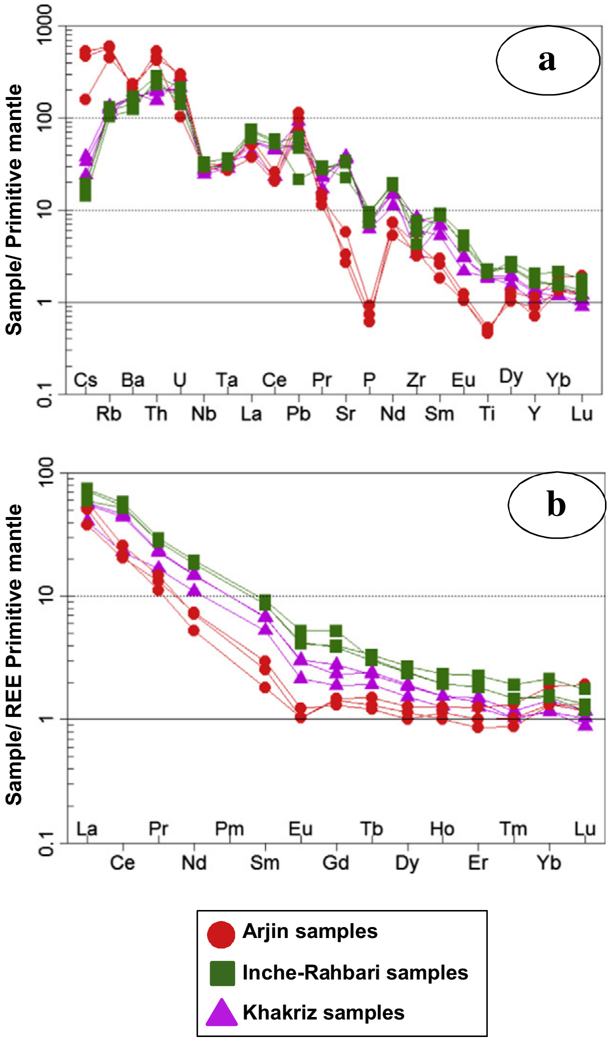

Fig. 9. (a) Primitive mantle-normalized multi-element variation diagram (McDonough and Sun, 1995) showing the main rock units of the KIAG intrusions. (b) Chondrite normalized REE diagram (McDonough and Sun, 1995) for the KIAG intrusions.

minerals such as forsterite, serpentine and talc do not occur in the Khakriz deposit.

5.1. Iron exoskarn

The main ore mineral in all deposits is magnetite, which is associated with minor amounts of hematite and sulfides (Fig. 6a, b, c, d). Magnetite is medium grained, euhedral to anhedral, and forms massive bodies, veinlets and disseminations in the skarns. In some cases, magnetite is oxidized to martite, goethite and limonite at surface.

Sulfide mineralization occurs as crosscutting veins and veinlets in the magnetite ore (Figs. 4f, 5c and 6b, c), and consists of pyrite, chalcopyrite, bornite and minor amounts of galena and sphalerite (Fig. 6b, c). The sulfide mineralization in the Inche-Rahbari deposit is less widespread than in the Arjin and Khakriz deposits. Pb-Zn mineralization is found only in the Khakriz deposit and is associated with chalcopyrite and pyrite. Chalcopyrite is closely associated with pyrite, and in some places with bornite as in the Arjin deposit (Fig. 6b, c). The sulfide minerals are usually altered to covellite, chalcocite, digenite, azurite, malachite, goethite and lepidocrocite.

Late-stage carbonate forms veins and veinlets up to 50 cm thick (Figs. 4c, 5f and 6). Late-stage carbonate veins cut the oxide, sulfide and other skarn minerals. These veins enclose fragments of magnetite, sulfide (pyrite and chalcopyrite), and skarn (Fig. 5f). Furthermore, late-stage carbonate veins are crosscut by hematite vein and veinlets up to 50 cm thick (Figs. 4e, 5f and 6d).

According to the mineral assemblage, the following events are distinguished in Zanjan skarn type iron deposits (Fig. 7): (1) prograde calcian and magnesian skarns and (2) retrograde skarns.

The prograde paragenesis in the calcic and magnesian skarns is made up by fine to coarse aggregates of light-brown garnets of the grossular-andradite series, forsterite (except for Khakriz deposit), and pyroxene (Fig. 6e, f).

Retrograde skarn forms lens- and vein- shaped masses within the prograde skarn bodies. Magnetite, serpentine, amphiboles of the tremolite-actinolite series (often asbestiform when pseudomorphing pyroxenes), chrysotile, talc, epidote, chlorite, calcite, quartz, hematite, pyrite, chalcopyrite and bornite are the dominant minerals in the retrograde skarn (Fig. 6g, h, i, j).

6. Classification of the KIAG intrusions

The whole-rock analyses of major and trace elements from all granite samples are listed in Table 1. We use the classification diagram of De la Roche et al. (1980). The samples plot in the fields of granite to quartz monzonite (Fig. 8a). All of the plutonic rock samples are metaluminous (Fig. 8b) and I-type (Fig. 8c) with an aluminum saturation index [ASI = molar $Al_2O_3/(CaO + K_2O + Na_2O)$] ranging from 0.8 to 1.1. All of the analyzed samples plot in the high-K calc-alkaline field of the K_2O-SiO_2 diagram (Fig. 8d). The SiO_2 contents of the KIAG analyzed samples range from ~67.14 to 76.7 wt% with a compositional gap between samples from Arjin and those from the Khakriz and Inche-Rahberi intrusions. The Arjin samples have chemical composition slightly different to those from other intrusions, with higher Rb, Th, Zr, Cs and La and lower Ni, Co, V, Y and Sr (Fig. 9). All the KIAG samples display similar trace element abundance patterns, with enrichment in LILE (e.g., Cs, Rb, and Th), depletion in HFSE and pronounced negative anomalies in Ta, Nb, Ti and P in the primitive mantle-normalized trace element spider diagram (McDonough and Sun, 1995; Fig. 9a). Rare earth element (REE) patterns show significant enrichment in light REE (LREE) and depletion in heavy REE (HREE), as indicated by the sloped pattern (Fig. 9b). They have a narrow range of Eu/Eu* ratios (Khakriz: 0.68–0.75; Inche-Rahbari: 0.70–0.76; Arjin: 0.53–0.64).

6.1. U-Pb age of the KIAG intrusions

Three samples from the KIAG intrusions including AJ-3 (Arjin granite), IN-4 (Inche-Rahbari quartz-monzonite) and KH-2 (Khakriz granodiorite) were selected for zircon U-Pb dating. The analytical results are presented in Table 2. The zircon grains have subhedral to euhedral shape (prismatic) and a light pink color with oscillatory zoning, indicating an igneous origin (Fig. 10).

Zircons from the Arjin granite sample (Aj-3) are transparent, 50–200 μm in length, and have aspect ratios of ~1:1 to 3:1 (Fig. 10). U and Th contents range from 558 to 1385 ppm, and from 417 to 1835 ppm, respectively; Th/U ratios vary between 0.329 and 0.614. The weighted mean $^{207}Pb/^{206}Pb$ age is calculated at 53 ± 1 Ma (MSWD = 1.7), which is interpreted as the crystallization age of this granite (Fig. 11a).

Zircons from Khakriz granodiorite sample (Kh-2) are transparent, pinkish in color, 50–250 μm in length, and have aspect ratios of ~1:1

Table 2
Zircon U-Pb analytical data of the KIAG intrusions.

Sample/spot #	Elements values					Row isotopic ratio				Radiogenic isotopic ratio#					Isotopic age (Ma)					
	[U] (ppm)	[Th] (ppm)	[Pb] (ppm)	Th/U (ppm)	f_{206}[a] (%)	$^{238}U/^{206}Pb$	±σ%	$^{207}Pb/^{206}Pb$	±σ%	$^{207}Pb/^{235}U$	±σ%	$^{206}Pb/^{238}U$	±σ%	ρ	$^{207}Pb/^{235}U$	±σ	$^{206}Pb/^{238}U$	±σ	$^{207}Pb/^{206}Pb$	±σ
Inche-Rahbari intrusion																				
IN-4-01	1742	1669	21	0.444	{0.28}	111.444	1.53	0.04964	1.38	0.05857	2.38	0.0089	1.53	0.64383	57.8	1.3	57.4	0.9	57.4	0.9
IN-4-02	1476	1182	17	0.371	{0.46}	110.623	1.59	0.04728	1.41	0.05893	2.12	0.009	1.59	0.74811	58.1	1.2	58	0.9	58	0.9
IN-4-03	786	955	10	0.564	{2.45}	117.666	1.64	0.06178	1.93	0.07239	2.54	0.0085	1.64	0.64821	71	1.7	54.6	0.9	53.5	0.9
IN-4-04	989	1123	12	0.526	{2.07}	120.452	1.72	0.05850	1.52	0.06696	2.29	0.0083	1.72	0.75029	65.8	1.5	53.3	0.9	52.5	0.9
IN-4-07	1097	779	12	0.329	{1.74}	119.703	1.51	0.05717	1.28	0.06585	1.97	0.0084	1.51	0.76287	64.8	1.2	53.6	0.8	52.9	0.8
IN-4-08	1071	924	14	0.4	{9.77}	113.000	1.52	0.09025	3.79	0.11012	4.08	0.0088	1.52	0.3732	106.1	4.1	56.8	0.9	53.7	0.9
IN-4-09	2917	3878	40	0.616	{5.90}	111.418	1.51	0.06268	3.04	0.07757	3.4	0.009	1.51	0.44396	75.9	2.5	57.6	0.9	56.5	0.9
IN-4-10	1053	897	12	0.395	{2.79}	118.150	1.61	0.05850	1.45	0.06826	2.16	0.0085	1.61	0.74344	67.1	1.4	54.3	0.9	53.5	0.9
IN-4-12	1414	1646	17	0.539	{0.20}	116.806	1.55	0.04737	1.45	0.05591	2.12	0.0086	1.55	0.73118	55.2	1.1	55	0.8	54.9	0.9
Arjin intrusion																				
AJ-3-03	558	417	6	0.347	{0.64}	118.624	1.54	0.04537	2.09	0.05274	2.59	0.0084	1.54	0.59261	52.2	1.3	54.1	0.8	54.2	0.8
AJ-3-07	830	815	10	0.455	{0.64}	119.218	1.52	0.04898	2.54	0.05665	2.96	0.0084	1.52	0.51401	56	1.6	53.8	0.8	53.7	0.8
AJ-3-08	681	483	7	0.329	{0.11}	117.897	1.59	0.04596	1.90	0.05375	2.48	0.0085	1.59	0.64055	53.2	1.3	54.4	0.9	54.5	0.9
AJ-3-10	1253	1380	15	0.51	{0.21}	123.565	1.51	0.04951	1.48	0.05511	2.08	0.0084	1.6	0.76636	54.5	1.1	54.1	0.9	54.1	0.9
AJ-3-12	949	853	10	0.417	{0.46}	123.256	1.55	0.04820	1.22	0.05525	2.12	0.0081	1.51	0.71472	54.6	1.1	52	0.8	51.8	0.8
AJ-3-13	1385	1835	17	0.614	{0.25}	118.701	1.60	0.04744	1.34	0.05392	1.97	0.0081	1.55	0.78673	53.3	1	52.1	0.8	52	0.8
AJ-3-16	659	511	7	0.36	{0.15}	120.559	1.54	0.04657	1.82	0.05326	2.38	0.0083	1.54	0.64507	52.7	1.2	53.3	0.8	53.3	0.8
Khakriz intrusion																				
KH-2-1	1830	3358	26	0.85	{0.10}	114.006	1.73	0.04678	1.47	0.05658	2.27	0.0088	1.73	0.76298	55.9	1.2	56.3	1	56.3	1
KH-2-02	681	646	8	0.44	{0.26}	120.636	1.67	0.04704	1.81	0.05376	2.46	0.0083	1.67	0.67936	53.2	1.3	53.2	0.9	53.2	0.9
KH-2-04	740	599	8	0.375	{0.40}	116.741	1.67	0.04866	1.81	0.05748	2.46	0.0086	1.67	0.67703	56.7	1.4	55	0.9	54.9	0.9
KH-2-05	696	363	7	0.242	{0.18}	115.313	1.55	0.04599	2.59	0.05499	3.02	0.0087	1.55	0.51392	54.4	1.6	55.7	0.9	55.7	0.9
KH-2-06	799	650	9	0.377	{0.20}	120.887	1.50	0.04968	1.68	0.05475	2.52	0.0083	1.5	0.59469	54.1	1.3	53	0.8	52.9	0.8
KH-2-07	1422	2190	19	0.714	{0.07}	114.698	1.58	0.04758	1.20	0.05652	2.04	0.0087	1.58	0.77088	55.8	1.1	55.9	0.9	55.9	0.9
KH-2-08	1874	913	58	0.226	{0.04}	38.496	1.50	0.04901	0.63	0.17442	1.64	0.026	1.5	0.91576	163.2	2.5	165.3	2.5	165.4	2.5
KH-2-09	1964	2268	24	0.535	{0.12}	115.200	1.50	0.04747	1.60	0.05567	2.33	0.0087	1.5	0.6441	55	1.2	55.7	0.8	55.7	0.8
KH-2-10	1192	1156	14	0.449	{0.22}	114.204	1.51	0.04827	1.33	0.0561	2.31	0.0087	1.51	0.65602	55.4	1.2	56.1	0.8	56.1	0.8
KH-2-11	1044	875	12	0.389	{0.20}	117.542	2.07	0.04718	1.45	0.05534	2.53	0.0085	2.07	0.81887	54.7	1.3	54.6	1.1	54.6	1.1
KH-2-12	595	417	7	0.325	{0.35}	114.954	1.60	0.04587	2.25	0.05502	2.76	0.0087	1.6	0.57885	54.4	1.5	55.8	0.9	55.9	0.9
KH-2-13	871	741	10	0.394	{0.15}	114.260	1.59	0.04697	1.57	0.05668	2.23	0.0088	1.59	0.71193	56	1.2	56.2	0.9	56.2	0.9
KH-2-14	567	367	6	0.3	{0.14}	116.138	1.95	0.04819	1.99	0.05584	3	0.0086	1.95	0.64875	55.2	1.6	55.2	1.1	55.2	1.1
KH-2-15	1096	1184	13	0.5	{0.32}	121.231	1.50	0.04744	1.44	0.05396	2.08	0.0082	1.5	0.72242	53.4	1.1	53	0.8	52.9	0.8
KH-2-16	639	383	7	0.278	{0.11}	116.448	1.53	0.04743	1.80	0.05505	2.54	0.0086	1.53	0.60315	54.4	1.3	55.1	0.8	55.1	0.8
KH-2-17	1047	951	12	0.421	{0.21}	114.556	1.51	0.04617	1.99	0.05557	2.5	0.0087	1.51	0.60365	54.9	1.3	56	0.8	56.1	0.8
KH-2-19	1325	1157	15	0.405	{0.46}	115.400	1.96	0.04934	1.44	0.05895	2.43	0.0087	1.96	0.80528	58.2	1.4	55.6	1.1	55.5	1.1
KH-2-20	607	379	6	0.289	{0.22}	116.552	1.57	0.04622	1.92	0.05468	2.48	0.0086	1.57	0.63254	54.1	1.3	55.1	0.9	55.1	0.9

[a] f_{206} is the percentage of common ^{206}Pb in total ^{206}Pb; # $^{207}Pb/^{235}U$ and $^{206}Pb/^{238}U$ are common Pb-corrected ratios. U-Th-Pb isotope ratios were calibrated relative to the seven standard Plěsovice zircons.

to 3:1 (Fig. 10). In CL images they are not homogeneous and show zoning. The U and Th contents of the Khakriz zircon grains are 595–1964 ppm and 363–3358 ppm, respectively; the Th/U ratios are 0.226–0.850. A weighted mean $^{207}Pb/^{206}Pb$ age is calculated at 55.3 ± 0.44 Ma (MSWD = 1.3), which is interpreted as crystallization age of this granodiorite (Fig. 11b).

Zircons from Inche-Rahbari quartz-monzonite sample (In-4) are transparent, 50–150 μm in length with aspect ratios of ~1:1 to 2: 1. In CL images the zircon grains show zoning (Fig. 10). These zircons have variable U (786–2917 ppm) and Th (779–3878 ppm) contents; and Th/U ratios between 0.329–0.616. Zircon grains from Inche-Rahbari granite show a bimodal age distribution. The minimum age of ca. 53 Ma is interpreted to date crystallization, and the older age of ca. 57 Ma to represent zircon xenocrysts trapped during magma ascent (Fig. 11c, d).

6.2. In situ zircon Hf and O isotopes

The LA-ICP-MS zircon Lu-Hf isotopic analyses of the KIAG intrusions are listed in Table 3 and supplementary material Table 1. The Arjin zircons show some variation in epsilon Hf (t) values ranging from −0.6 to +5.8 (Fig. 12a). The εHf values of the Inche-Rahbari zircons are +1.0 to +3.4 and εHf values of −0.7 to +4.0 were obtained from Khakriz zircon grains (Fig. 12c, e) suggesting the εHf values of these granite at the time of emplacement. Furthermore, two-stage model ages were calculated for the granitic zircon grains in the study area ranging from 1052 to 1624 Ma for the Arjin granite, 1266 to 1632 Ma for the Inche-Rahbari quartz-monzonite and 1214 to 1640 Ma for the Khakriz granodiorite (Table 3 and supplementary material Table 1). The measured $^{176}Hf/^{177}Hf$ and $^{176}Lu/^{177}Hf$ of the zircons were used to calculate the two-stage model age (T^{c}_{DM}) that is related to sample via

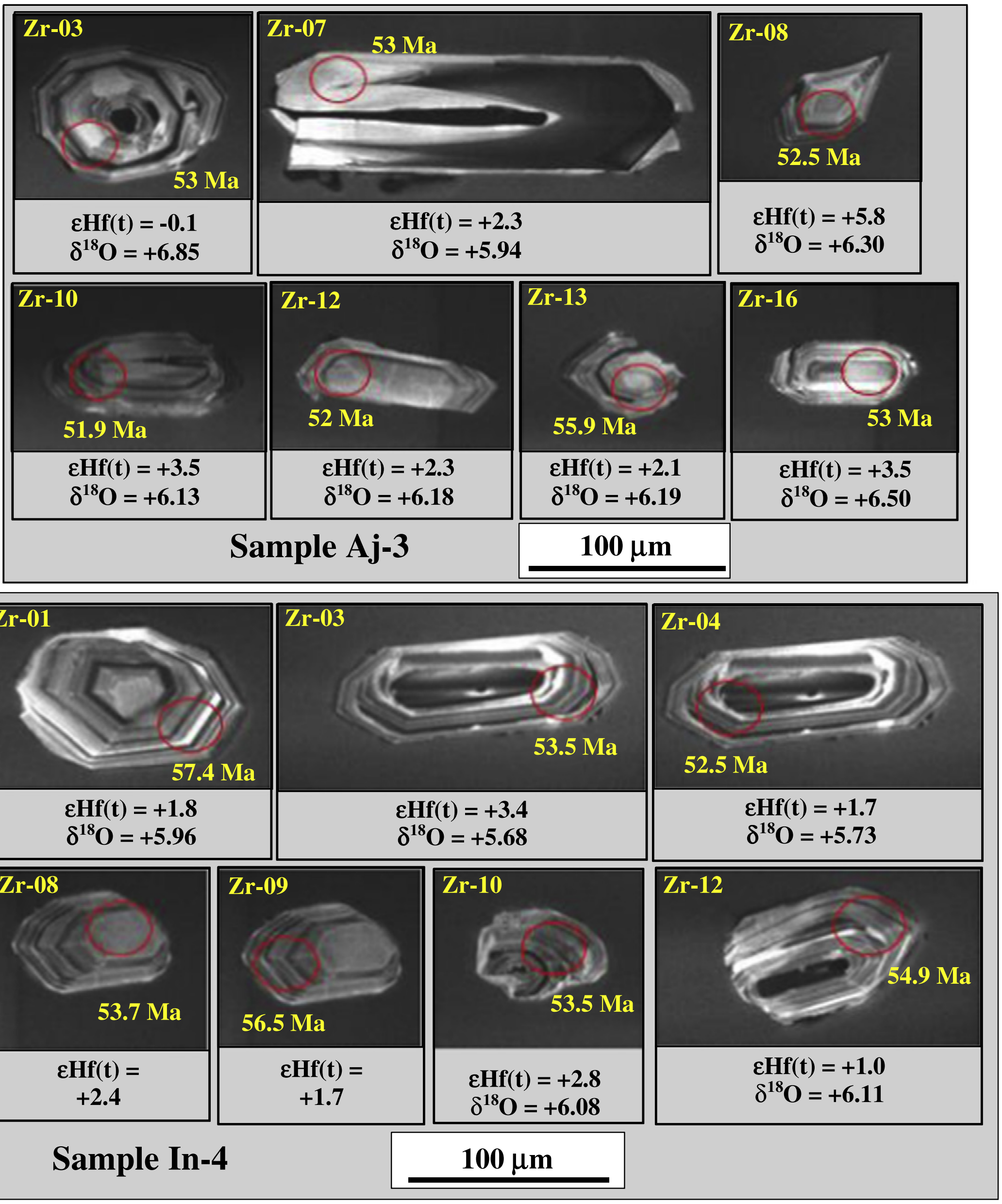

Fig. 10. Cathodoluminiscence (CL) images of representative zircon crystals used for U-Pb dating from the Arjin (sample Aj-3), Inche-Rahbari (In-4) and Khakriz (Kh-2) granites.

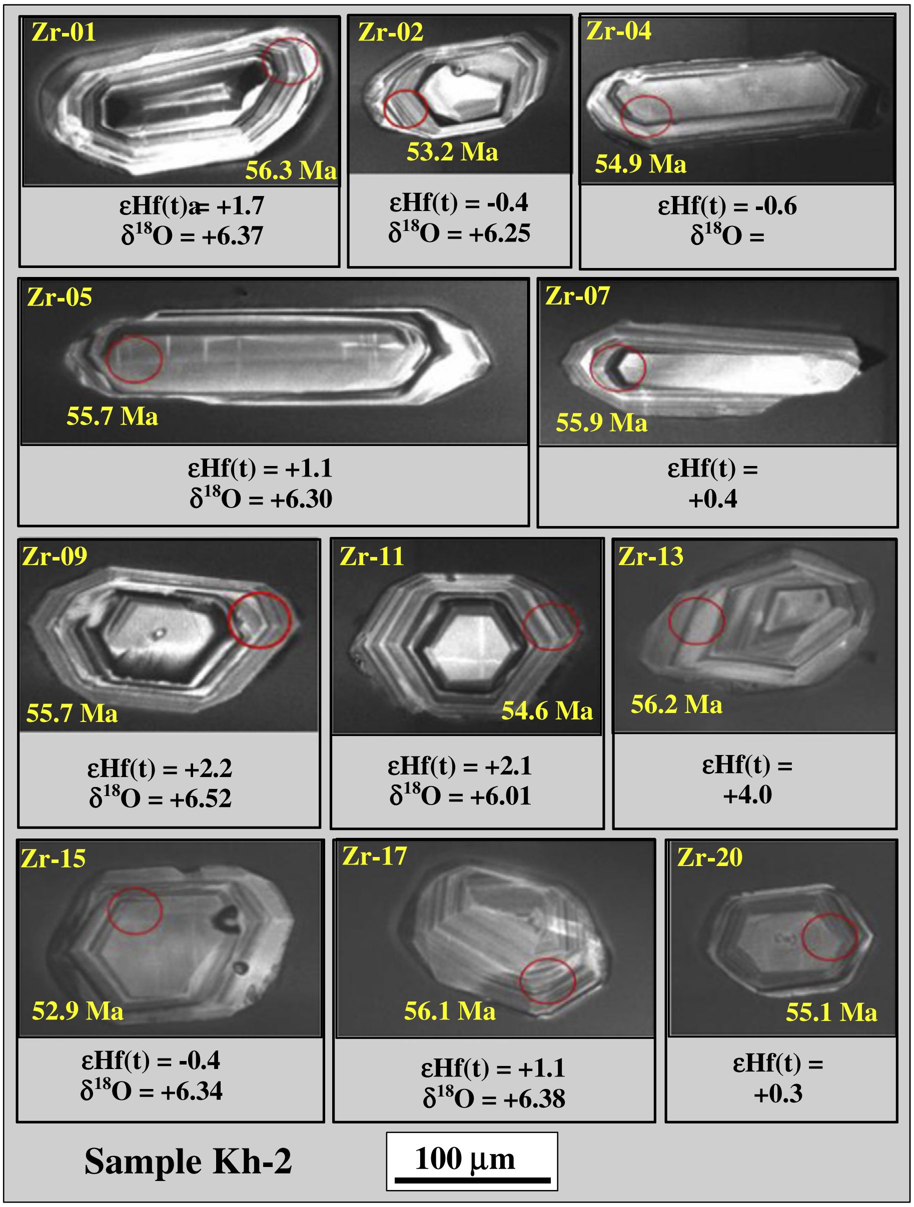

the lower crust following derivation from depleted mantle (e.g. Li et al., 2013).

The results of SIMS $\delta^{18}O$ analyses of the zircon grains for three samples from the Arjin, Inche-Rahbari and Khakriz granites are presented in Table 4. The measured zircon $\delta^{18}O$ values are 5.8‰ to 7.42‰ for the Arjin granite, 5.68 to 6.13‰ for the Inche-Rahbari quartz-monzonite and 5.55 to 6.69‰ for the Khakriz granodiorite (Fig. 12b, d, f).

6.3. Stable isotopes (S, O and C)

Sulfur isotopic compositions were determined in chalcopyrite and pyrite. Sulfide minerals are sparsely present in the Zanjan skarn type iron deposits. In total, 19 samples were provided for sulfur isotope analysis. Samples from the Arjin deposit return $\delta^{34}S$ values in the range from +15.99 to +18.35‰; those from the Inche-Rahbari and Khakriz deposits are between +2.96 to +5.30‰ (Table 5).

The results of the analyses of $\delta^{18}O$ and $\delta^{13}C$ in carbonate are listed in Table 6. Calcite and dolomite from the host rock (Soltanyeh Formation) of the Arjin deposit, near the mineralized zones, give $\delta^{18}O$ values of +11.59 to +19.47‰ and $\delta^{13}C$ values of −1.4 to +1.27‰ (Table 6). The $\delta^{18}O$ and $\delta^{13}C$ values for host rock carbonates far from mineralized zones are +23.74 to +24.41‰ and −0.06 to −0.64‰, respectively. Calcite and dolomite from the late stage hydrothermal carbonates in the Arjin deposit give $\delta^{18}O$ values of +6.49 to +20.67‰ and $\delta^{13}C$ values of −2.86 to +1.86‰ (Table 6). The $\delta^{18}O$ and $\delta^{13}C$ values for host rocks of the Inche-Rahbari and Khakriz deposits are +19.57 to +20.63‰ and −0.48 to +0.03‰, respectively (Table 6). These carbonate samples are far from ore

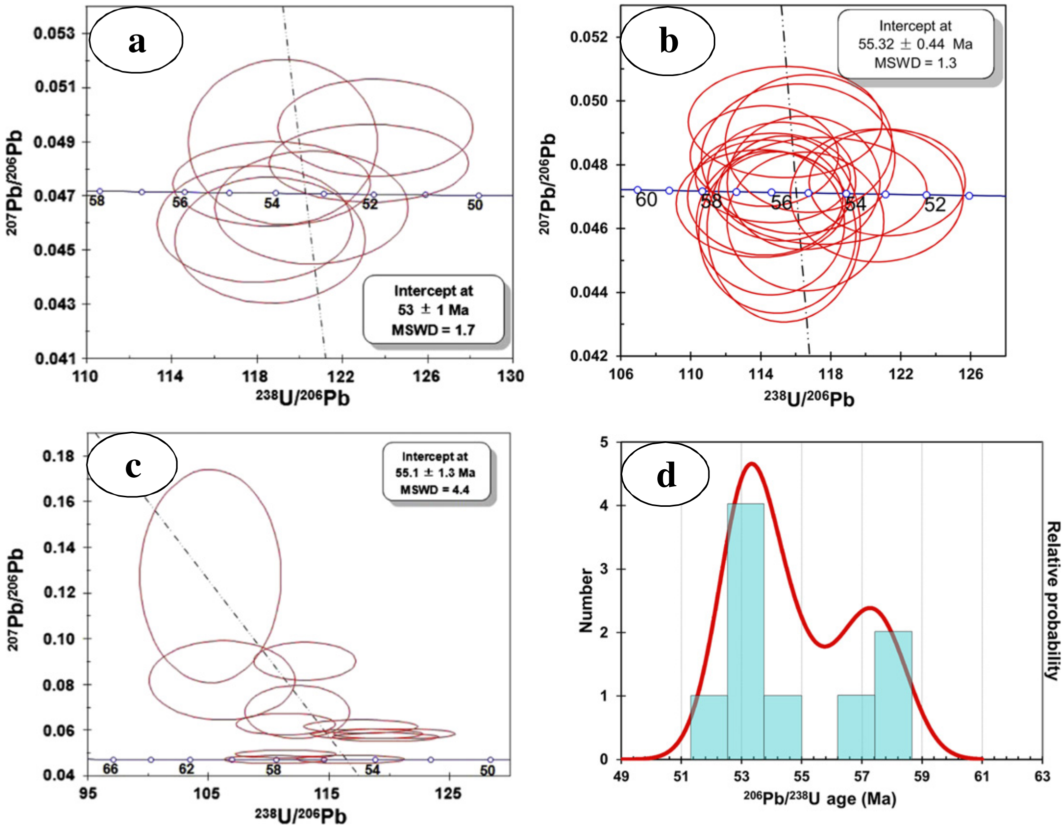

Fig. 11. Inverse U-Pb concordia diagrams of zircon spot analyses from representative plutonic rocks of the KIAG suite; (a) Arjin (sample Aj-3); (b) Khakriz (sample Kh-2); (c) mean age from two populations in the Inche-Rahbari sample (sample In-4); (d) bimodal Pb-Pb ages of zircons from the Inche-Rahbari intrusion (sample In-4). The error ellipses and the errors of the mean ^{207}Pb/^{206}Pb ages are 2-sigma.

zones. The host rock carbonate from these deposits near the ore deposits give δ^{18}O values of +21.53 to +23.08‰ and δ^{13}C values of −9.67 to +2.21‰ (Table 6). The late stage hydrothermal calcites from Inche-Rahbari and Khakriz deposits give δ^{18}O values of +3.29 to +8.94‰ and δ^{13}C values of −5.32 to −4.12‰ (Table 6).

7. Discussion

7.1. Role of the Cenozoic plutonism

The KIAG suite was formed by multiple intrusion of granitoid magmas during early Eocene time. These plutonic rocks with compositions of quartz-monzonite, granodiorite and granite are characterized by approximately similar chondrite-normalized REE and trace elements pattern as well as zircons Lu-Hf and oxygen isotopic compositions, suggesting a common source. The early Eocene intrusions are calc-alkaline, metaluminous and I-type with HFSE depletion (Nb, Y, Ta, Ti) and LILE (Ba, Th, Rb, U, and K) enrichment similar to both arc-related mantle-derived magmas and crustal-derived melts. However, the SiO_2 and Mg# values (Table 1) of KIAG intrusions are not consistent with magmas produced by partial melting of metasomatized mantle. Fractionation of clinopyroxene and hornblende is supported by HREE depletion and a lack of europium anomaly in the Khakriz and Inche-Rahbari samples. The Aarjin samples, however, show relatively high values of Rb/Sr and negative europium anomalies suggesting plagioclase fractionation during magmatic evolution.

In addition to geochemical data, we used zircon Hf-O isotopic analyses from the KIAG intrusions to constrain their petrogenesis. According to Belousova et al. (2010) zircon is the principal host for Hf. The low Lu/Hf ratios of zircon and its resistance to isotopic disturbance make it ideal for both U-Pb geochronology and Lu-Hf isotope analysis (Goodge and Vervoort, 2006; Belousova et al., 2006, 2010; Lenting et al., 2010). Oxygen isotopes in zircon are also a suitable to identify the possible role of supracrustal components in the origin and the evolution of magmas (Valley, 2003; Valley et al., 2005; Zheng et al., 2006; Be′eri-Shlevin et al., 2010). The KIAG zircon grains are characterized by initial Hf ratios ($\varepsilon Hf_{(t)}$ of −0.7 to +5.8; Fig. 13a) that are lower than those predicted for a depleted mantle value at ~50 Ma (Fig. 13a). Moreover, the zircon δ^{18}O values of the KIAG intrusions (Fig. 13b) are higher (spatially in the Arjin zircons) than those reported for mantle-derived melts (~5.3‰; Valley et al., 1998), thus suggesting a variable contribution of ^{18}O-enriched crustal material. Zircons with high δ^{18}O and $\varepsilon Hf_{(t)}$ below the range of depleted mantle suggest a contribution of preexisting igneous rocks in the genesis of KIAG magmas (Fig. 13c).

The δ^{18}O values of KIAG zircons fall into the range of zircons from I-type granites (5–8‰; Li et al., 2007) and are comparable with those from Caledonian I-type granites in Australia (δ^{18}O zircon of 6–8.5‰; Kemp et al., 2009).

Furthermore, zircon grains in the KIAG samples yielded T_{DM2} ages from 1052 to 1640 Ma which are similar to those reported from Neoproterozoic granites and gneisses in the Central Iran and Sanandaj-Sirjan zones (T_{DM} = 1.0–2.0 Ga; Balaghi Einalou et al., 2014; Nutman et al., 2014; Shafaii Moghadam et al., 2016) and suggest the

Table 3

Summary of Lu-Hf isotope compositions of zircons from the KIAG intrusions.

Sample	Age (Ma)	$e_{Hf}(0)$	$e_{Hf}(t)$	2σ	T_{DM1}(Hf) (Ma)	T^{C}_{DM} (Ma)
Khakriz intrusion						
KH-2-01	55	0.6	1.7	0.78	665	1018
KH-2-02	55	−1.6	−0.4	0.73	745	1154
KH-2-03	55	−1.8	−0.6	0.69	752	1167
KH-2-04	55	−0.1	1.1	0.69	682	1061
KH-2-05	55	1.5	2.6	0.88	626	962
KH-2-06	55	−0.8	0.4	0.66	714	1105
KH-2-08	55	1	2.2	0.83	640	989
KH-2-09	55	1.2	2.4	1.09	635	978
KH-2-10	55	1	2.1	0.83	643	992
KH-2-11	55	−0.5	0.7	0.83	689	1081
KH-2-12	55	2.8	4	1.03	583	874
KH-2-13	55	−1.9	−0.7	0.87	754	1173
KH-2-14	55	−1.5	−0.4	0.97	742	1149
KH-2-15	55	0.8	2	0.85	644	1000
KH-2-16	55	−0.1	1.1	0.89	689	1061
KH-2-17	55	−1.1	0.1	0.99	724	1121
KH-2-18	55	−0.9	0.3	0.86	716	1110
Arjin intrusion						
AJ-3-01	53	0.2	1.3	0.71	675	1043
AJ-3-02	53	−1.2	−0.1	0.73	734	1131
AJ-3-04	53	1.2	2.3	0.81	628	978
AJ-3-05	53	−0.7	0.4	0.87	712	1100
AJ-3-06	53	1	2.1	0.7	644	991
AJ-3-07	53	−1.7	−0.6	1.55	753	1161
AJ-3-08	53	4.6	5.8	1.33	495	759
AJ-3-10	53	2.4	3.5	1.37	586	904
AJ-3-12	53	1.2	2.3	1.61	640	980
AJ-3-13	53	1	2.1	1.46	642	990
AJ-3-14	53	0.8	1.9	0.88	657	1005
AJ-3-15	53	3.1	4.3	1.37	552	854
AJ-3-17	53	2.4	3.5	1.6	583	903
Incheh-Rahbari intrusion						
IN-4-01	55	0.6	1.8	0.84	661	1013
IN-4-03	55	2.3	3.4	0.93	608	909
IN-4-04	55	0.6	1.7	1.02	678	1017
IN-4-05	55	−0.1	1	1	692	1064
IN-4-06	55	0.7	1.8	0.82	658	1011
IN-4-07	55	0.6	1.7	1.26	686	1016
IN-4-08	55	2.2	3.4	0.96	602	912
IN-4-11	55	−1.8	−0.6	1.05	756	1167
IN-4-12	55	1.2	2.4	0.87	630	974
IN-4-13	55	1.7	2.8	0.92	622	949
IN-4-15	55	0.4	1.5	0.98	689	1029
IN-4-16	55	−0.1	1	0.83	691	1061
IN-4-18	55	1.1	2.3	1.11	650	983
IN-4-19	55	1.4	2.6	1.03	629	964

The chondritic ratios of $^{176}Hf/^{177}Hf$ (0.282772) and $^{176}Lu/^{177}Hf$ (0.0332) (Blichert-Toft and Albarède, 1997) were used to calculate εHf values. Single-stage Hf model ages (T_{DM1}) were calculated using the measured ratios, referred to a model depleted Mantle with present-day $^{176}Hf/^{177}Hf$ of 0.28325 and $^{176}Lu/^{177}Hf$ of 0.0384 (Vervoort and Blichert-Toft, 1999). Two-stage Hf model ages (T_{DMC}) were calculated assuming a mean $^{176}Lu/^{177}Hf$ value of 0.015 for average continental crust (Amelin et al., 1999; Griffin et al., 2002). The $^{176}Hf/^{177}Hf$ ratios were calibrated relative to the ten zircon standards MUD and five GJ1.

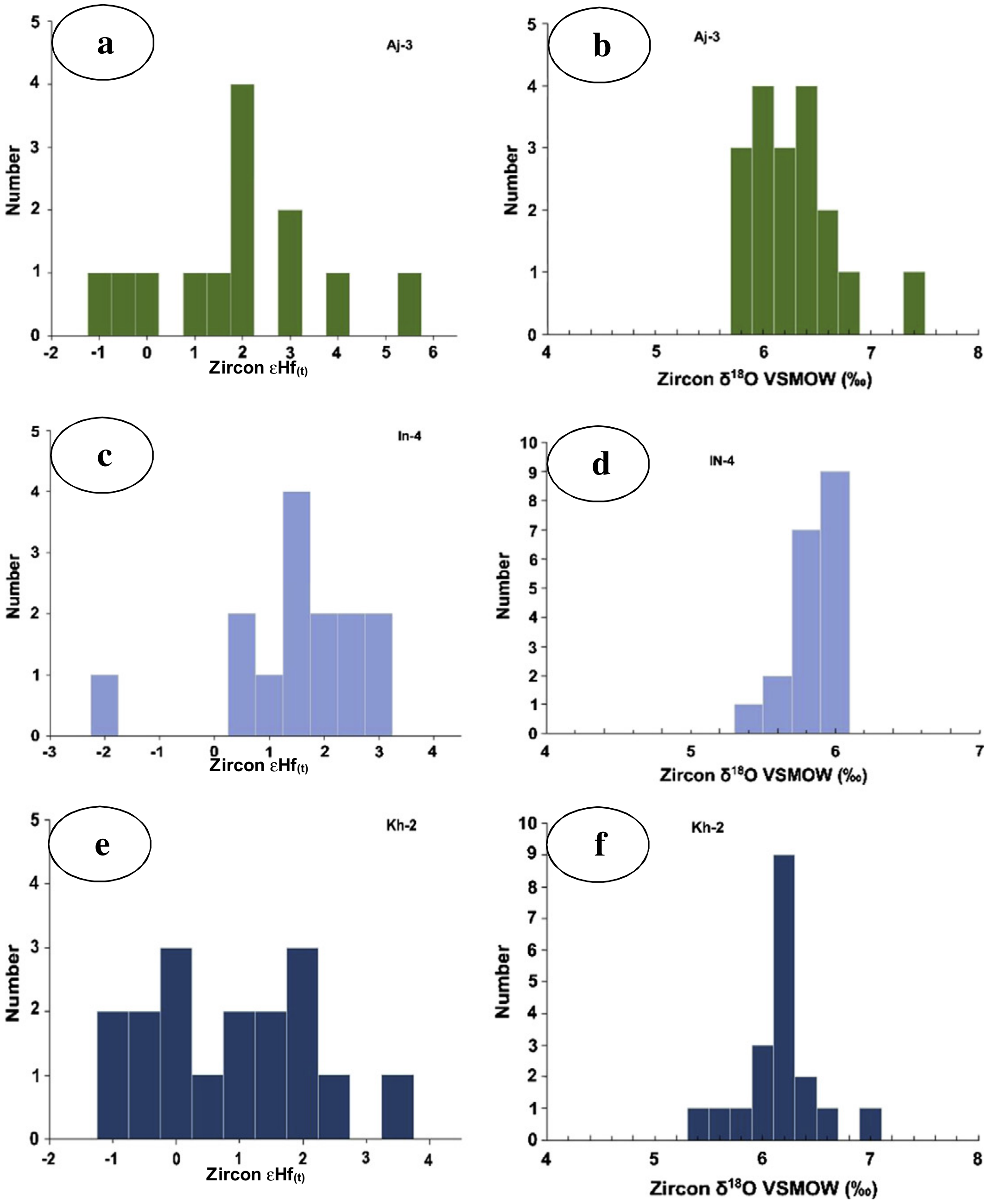

Fig. 12. Histograms of zircon ε_{Hf}(t) and δ^{18}O values of the KIAG intrusive suite. (a) zircon ε_{Hf}(t) values Arjin granite; (b) zircon δ^{18}O values Arjin granite; (c) zircon ε_{Hf}(t) values Inche-Rahbari granite; (d) zircon δ^{18}O values Inche-Rahbari granite; (e) zircon ε_{Hf}(t) values Khakriz granite; (f) zircon δ^{18}O values Khakriz granite.

contribution of old crust (Paleoproterozoic?) in their genesis (Fig. 13a). The geochemical features and the zircon $\varepsilon Hf_{(t)}$ of the KIAG intrusions suggest involvement of different proportions of mafic-intermediate old continental rocks mixed with a juvenile component. Moreover, the δ^{18}O values of the KIAG zircons suggest assimilation of magmas with supracrustal material, which is more appreciated in the Arjin granite (Fig. 13b). Thus, the zircon Hf and O isotopes in the studied granitoids show that the KIAG intrusions are the mixtures of mantle-derived, juvenile melts with older continental crust which underwent different proportions of crustal contamination during ascending and emplacement in the upper crust. Consequently, the high-K calc-alkaline I-type KIAG intrusions can be generated by underplating of mafic magmas near the lower continental crust which supply sufficient heat for partial melting of the lower crust (e.g., Hildreth, 1981).

There was widespread igneous activity during the Eocene to Oligocene in central Iran as well in the Urumieh-Dokhtar magmatic arc (UDMA), Alborz and East of Iran (Verdel et al., 2007; Kargaranbafghi et al., 2012; Asiabanha and Foden, 2012; Verdel et al., 2011; Chiu et al., 2013; Honarmand et al., 2014; Nabatian et al., 2014). These igneous rocks are typical of continental arc magmatism including metasomatized mantle-derived magmas and continental partial melts. Subduction of Neotethyian oceanic crust

Table 4
Oxygen isotopic compositions of zircons from the KIAG intrusions.

Sample	$^{16}O/^{18}O$ mean	delta ^{18}O	2SE
Incheh-Rahbari intrusion			
In-4-1	0.002014796	5.96	0.27
In-4-2	0.002014766	5.94	0.23
In-4-3	0.002014244	5.68	0.18
In-4-4	0.002014346	5.73	0.23
In-4-5	0.002014892	6.00	0.24
In-4-6	0.002014905	6.01	0.26
In-4-7	0.002014030	5.57	0.28
In-4-8	0.002014973	6.04	0.23
In-4-9	0.002015069	6.09	0.27
In-4-10	0.002015139	6.13	0.28
In-4-11	0.002014669	5.89	0.21
In-4-12	0.002014636	5.88	0.32
In-4-13	0.002015052	6.08	0.22
In-4-14	0.002014973	6.04	0.26
In-4-15	0.002014907	6.01	0.30
In-4-16	0.002015097	6.11	0.27
In-4-17	0.002014585	5.85	0.16
In-4-18	0.002014680	5.90	0.17
In-4-19	0.002014545	5.83	0.19
Arjin intrusion			
Aj-3-1	0.002016673	7.42	0.55
Aj-3-2	0.002015517	6.85	0.36
Aj-3-3	0.002014863	6.52	0.34
Aj-3-4	0.002013693	5.94	0.28
Aj-3-5	0.002013409	5.80	0.31
Aj-3-6	0.002014300	6.24	0.31
Aj-3-7	0.002013758	5.97	0.26
Aj-3-8	0.002014424	6.30	0.21
Aj-3-9	0.002015674	6.92	0.24
Aj-3-10	0.002014077	6.13	0.31
Aj-3-11	0.002014769	6.47	0.22
Aj-3-12	0.002014190	6.18	0.24
Aj-3-13	0.002014192	6.19	0.30
Aj-3-14	0.002015440	6.81	0.33
Aj-3-15	0.002014403	6.29	0.25
Aj-3-16	0.002014673	6.43	0.32
Aj-3-17	0.002014819	6.50	0.34
Aj-3-18	0.002013823	6.00	0.25
Khakriz intrusion			
KH-2-1	0.002014570	6.37	0.27
KH-2-2	0.002014265	6.22	0.29
KH-2-3	0.002014330	6.25	0.29
KH-2-4	0.002015207	6.69	0.20
KH-2-5	0.002014631	6.40	0.30
KH-2-6	0.002014429	6.30	0.20
KH-2-7	0.002015235	6.05	0.26
KH-2-8	0.002014472	5.67	0.20
KH-2-9	0.002017234	7.05	0.27
KH-2-10	0.002014222	5.55	0.32
KH-2-11	0.002016163	6.52	0.30
KH-2-12	0.002015156	6.01	0.13
KH-2-13	0.002015444	6.16	0.26
KH-2-14	0.002016488	6.68	0.33
KH-2-15	0.002015050	5.96	0.20
KH-2-16	0.002015809	6.34	0.22
KH-2-17	0.002015800	6.33	0.23
KH-2-18	0.002015886	6.38	0.31
KH-2-19	0.002016154	6.51	0.26
KH-2-20	0.002015760	6.31	0.20

The instrumental mass fractionation factor was corrected using 12 standard zircons Penglai, and the 6 Qinghu zircon was used for quality control.

beneath the Iranian plateau played an important role in generating such Andean-type arc-magmatism before continental collision in the Zagros.

7.2. Source of ore-forming fluids

According to Bowman (1998) magmatic fluids are the source of sulfur in most skarn deposits. Sulfur isotope values close to delta $^{34}S = 0‰$ are interpreted by Spiro and Puig (1988) and Seal (2006) as indicative of a magmatic source.

Sulfur isotope analyses of sulfides (pyrite and chalcopyrite) were carried out on optically pure mineral separates associated with massive and banded magnetite. The $\delta^{34}S$ values of sulfide samples from the Arjin deposit range from +15.99 to +18.35‰ (Fig. 14a). The $\delta^{34}S$ values of 9 pyrite samples from Inche-Rahbari and Khakriz deposits range from +2.96 to +5.30‰ (Fig. 14a). These $\delta^{34}S$ values of sulfide minerals in the latter two deposits are

Table 5
Sulfur isotope data of the Khakriz, Inche-Rahbari and Arjin iron skarn deposits.

Sample	Mineral	Description	$\delta^{34}S$ (CDT)	σ ($\delta^{34}S$)	% S
Arjin deposit					
GNA-6	Pyrite	Late stage sulfide vein	17.12	0.07	52.4
GNA-7	Pyrite	Disseminate pyrite associated with magnetite	16.81	0.07	52.2
GNA-7	Pyrite	Disseminate pyrite associated with magnetite	17.02	0.07	49.3
GNA-9	Pyrite	Late stage sulfide vein	15.99	0.07	51.1
GNA-9	Chalcopyrite	Late stage sulfide vein	16.06	0.07	34.8
GNA-10	Pyrite	Late stage sulfide vein	16.3	0.07	54.3
GNA-11	Pyrite	Late stage sulfide vein (banded magnetite mineralization)	17.82	0.07	52.8
GNA-11	Chalcopyrite	Late stage sulfide vein (banded magnetite mineralization)	16.3	0.07	31.1
GNA-12	Pyrite	Late stage sulfide vein (banded magnetite mineralization)	17.56	0.07	52.9
GNA-13	Pyrite	Late stage sulfide vein	18.35	0.07	50.3
GNA-15	Pyrite	Late stage sulfide vein	17.48	0.07	51.4
Incheh-Rahbari deposit					
GN-IN-1	Pyrite	Late stage sulfide vein	4.29	0.07	47.6
GN-IN-10	Pyrite	Late stage sulfide vein	2.96	0.07	50.1
GN-IN-13	Pyrite	Late stage sulfide vein (massive texture)	4.8	0.07	51.2
GN-IN-15	Pyrite	Late stage sulfide vein (massive texture)	5.3	0.07	49.9
Khakriz deposit					
GN-KH-1	Pyrite	Late stage sulfide vein (cutting the host rock and garnet zone)	5.04	0.07	51.1
GN-KH-2	Pyrite	Late stage sulfide vein (cutting the host rock and garnet zone)	4.78	0.07	50.4
GN-KH-8	Pyrite	Late stage sulfide vein (cutting the hornfels host rock)	4.01	0.07	50.8
GN-KH-10	Pyrite	Late stage sulfide vein (cutting the ore body)	4.97	0.07	52.6
GN-KH-12	Pyrite	Late stage sulfide vein (cutting the host rock)	4.2	0.07	48.4

The $\delta^{34}S$ ratios were calibrated using the IAEA S1, IAEA S2, IAEA S3 and NBS-123 international standards. The analytical error was less than 1.5.

similar to those from sulfide minerals in Fe skarn deposits worldwide (Rose et al., 1985; Shen et al., 2013; Xie et al., 2015). The relatively large range of $\delta^{34}S$ values in this study (Table 5 and Fig. 14a), however, suggest that there are different sources or different mechanisms affecting the sulfur species from such a magmatic source. Considering the isotope composition of sulfide minerals from the Inche-Rahbari and Khakriz Fe skarn deposits we propose that sulfur originated from dominantly magmatic fluids (Ohmoto and Rye, 1979) with minor contributions from meteoric water. However, the $\delta^{34}S$ values in the Arjin deposit suggest interaction of magmatic hydrothermal fluids with carbonate host rocks as the main process in ore mineralization. According to Bowman (1998), variations in the $\delta^{34}S$ values of sulfide minerals in the skarn deposits indicate progressive contributions of wallrock sulfur or changes in physico-chemical conditions of the skarn fluids.

According to Shimazaki et al. (1986), the carbon and oxygen isotopic composition of the fluids during the later stages of skarn mineralization, can be obtained by isotopic analysis of calcite. There are three main sources for carbon in the ore-forming

Table 6
Oxygen and carbon isotope data of the Khakriz, Inche-Rahbari and Arjin iron skarn deposits.

Sample	Mineral	Description	$\delta^{13}C$ (PDB)	$\sigma(\delta^{13}C)$	$\delta^{18}O$ (PDB)	$\delta^{18}O$ (SMOW)	$\sigma(\delta^{18}O)$
Arjin deposit							
GNA-1	Calcite	Late-stage carbonate	−2.09	0.04	−23.08	7.07	0.07
GNA-2	Calcite	Late-stage carbonate	−2.01	0.04	−22.48	7.69	0.07
GNA-3	Calcite	Late-stage carbonate	−2.86	0.04	−23.64	6.49	0.07
GNA-4	Dolomite	Late-stage carbonate	−2.15	0.04	−19.58	10.67	0.07
GNA-5	Calcite	Late-stage carbonate	−2.45	0.04	−24.50	5.61	0.07
GNA-17	Dolomite	Late-stage carbonate	1.86	0.04	−9.89	20.67	0.07
GNA-16	Calcite	Host rock carbonate (near the mineralization)	−1.40	0.04	−18.69	11.59	0.07
GNA-18	Dolomite	Host rock carbonate (near the mineralization)	1.27	0.04	−11.05	19.47	0.07
GNA-19	Dolomite	Host rock (far from mineralization)	−0.64	0.04	−6.91	23.74	0.07
GNA-20	Dolomite	Host rock (far from mineralization)	−0.06	0.04	−6.26	24.41	0.07
Inche-Rahbari deposit							
GN-I1	Calcite	Host rock dolomite (far from ore deposit)	−0.48	0.04	−10.95	19.57	0.07
GN-I2	Calcite	Host rock dolomite	0.03	0.04	−17.21	13.12	0.07
GN-I4	Calcite	Recrystalization of host rock dolomite (near the mineralization)	−9.67	0.04	−9.05	21.53	0.07
GN-IN5	Calcite	Late-stage carbonate	−5.02	0.04	−21.26	8.94	0.07
GN-IN6	Calcite	Late-stage carbonate	−4.12	0.04	−22.61	7.56	0.07
Khakriz deposit							
GN-I3	Dolomite	Host rock dolomite (far from ore deposit)	−0.10	0.04	−9.93	20.63	0.07
GN-KH4	Calcite	Late-stage carbonate	−5.16	0.04	−26.75	3.29	0.07
GN-KH6	Calcite	Late-stage carbonate (cutting the host rock and ore deposit)	−5.32	0.04	−25.16	4.92	0.07
GN-KH7	Calcite	Host rock dolomite (near the ore deposit)	2.21	0.04	−7.55	23.08	0.07

Results were calibrated with the NBS-18 and NBS-19 international standards. The analytical error are less than 0.02 for $\delta^{13}C$ and 0.06 for $\delta^{18}O$.

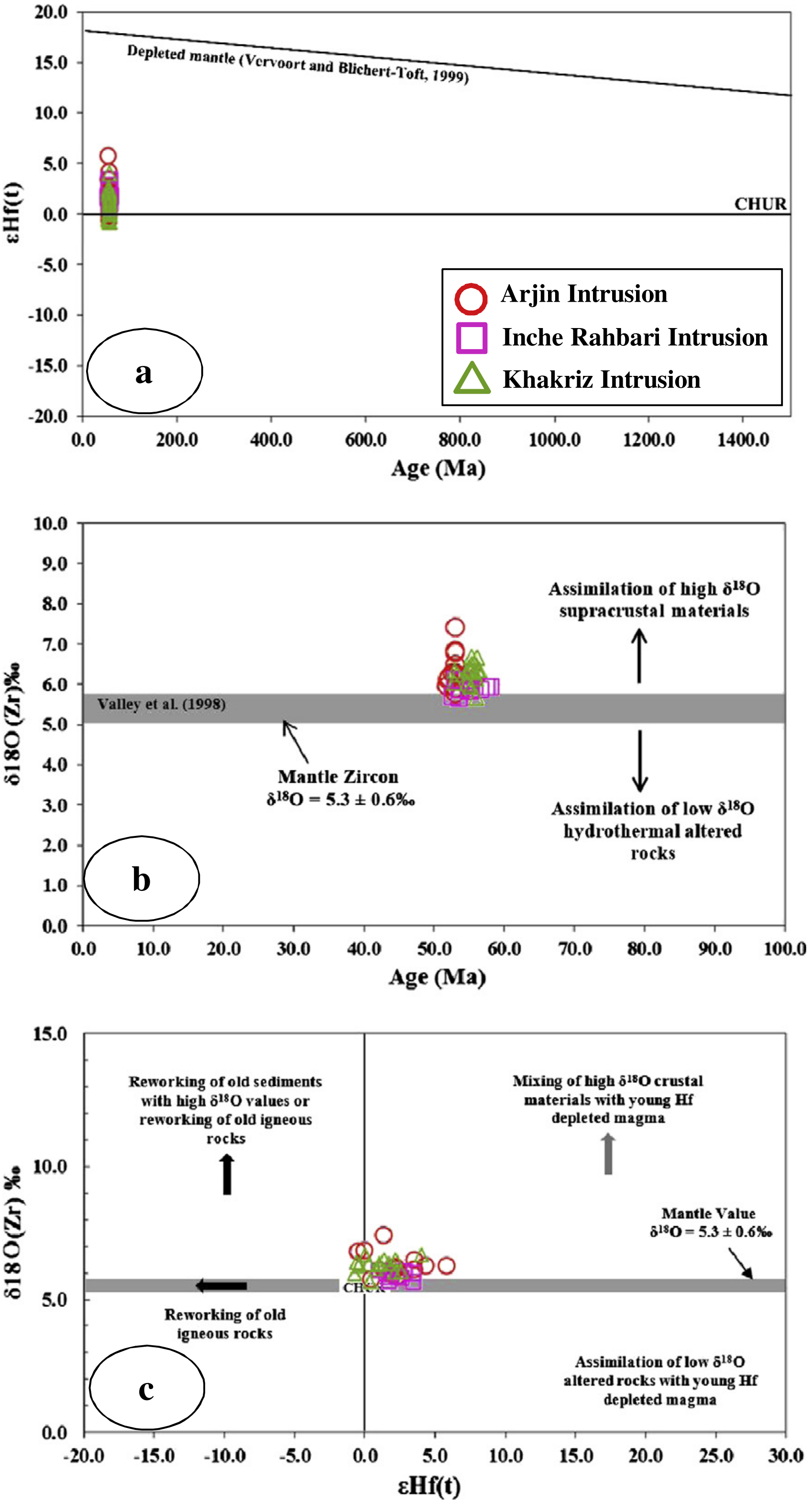

Fig. 13. (a) Epsilon Hf (t) versus zircon age diagram showing the zircon data for Arjin, Khakriz and Inche-Rahbari granitic rocks and the depleted mantle (DM) curve from a chondritic uniform reservoir (CHUR) at the Earth's formation to epsilon Hf = 18 at the present time (Vervoort and Blichert-Toft, 1999). (b) Single zircon $\delta^{18}O$ data versus age from the Eocene KIAG granites. Field of mantle zircon from Valley et al. (1998); (c) Single zircons epsilon Hf (t) versus $\delta^{18}O$ data from KIAG granites. All epsilon Hf (t) values were calculated with CHUR values of $^{176}Hf/^{177}Hf$ (0.282772) and $^{176}Lu/^{177}Hf$ (0.0332) as reported by Blichert-Toft and Albarède (1997) and a ^{176}Lu decay constant (λ) of 1.867×10^{-11} as reported by Scherer et al. (2001).

fluids: a) mantle-derived or magma-derived carbon, with isotopic values of carbon ($\delta^{13}C_{V\text{-}PDB}$) varying from −5‰ to −2‰ or from −9‰ to −3‰, respectively (Taylor, 1986); b) carbon derived from dissolution of carbonate in sediments or by interaction between brine and mudstone, with carbon isotopic composition ranging from −2‰ to +3‰, whereas seawater $\delta^{13}C_{V\text{-}PDB}$ values

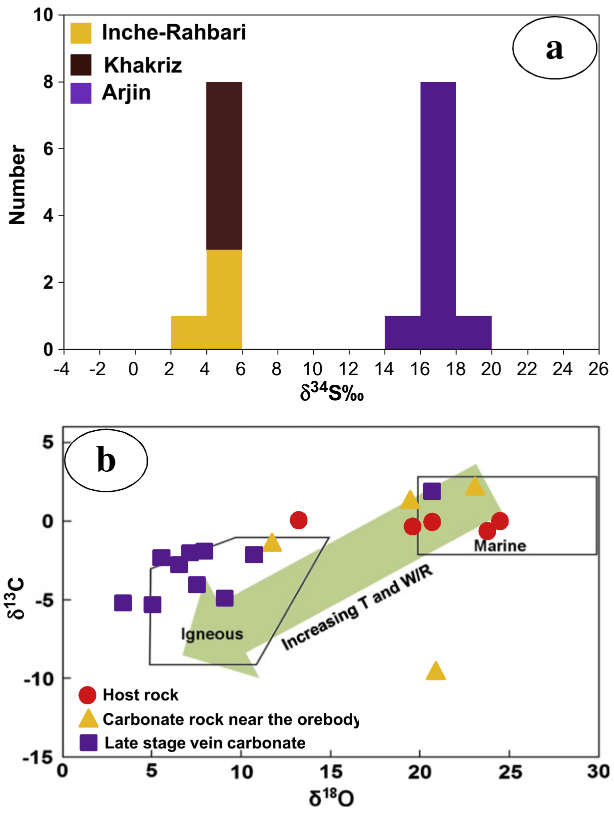

Fig. 14. (a) Histogram of sulfur isotopes in pyrite and chalcopyrite from Arjin, Inche-Rahbari and Khakriz Fe skarn deposits in the Zanjan district; (b) Carbon-oxygen isotopic composition of the Arjin, Inche-Rahbari and Khakriz Fe skarn deposits. Carbon and oxygen isotope data of igneous calcite and marine carbonates are from Ray et al. (2000) and Zheng (2001), respectively. The green arrow shows increasing of temperature (T) and water/rock (W/R) interactions (Ren et al., 2015). (For interpretation of the references to color in this figure legend, the reader is referred to the web version of this article.)

remain near 0‰ (Veizer et al., 1980); c) carbon derived from various organic materials enriched in ^{12}C, with isotopic composition of carbon ($\delta^{13}C_{V\text{-}PDB}$) is very low, ranging from −30‰ to −15‰ (Ohmoto, 1972).

Based on isotopic composition of carbon at the Arjin, Inche-Rahbari and Khakriz deposits, C content of unaltered host rock carbonate ranges from −0.64‰ to +0.03‰, and is likely derived from sedimentary carbonate.

However, the simple de-carbonation and dissolution of the host marine carbonates is well consistent with the scale of the δ^{13}C depletion observed in the Zanjan skarns and ores (Fig. 14b). The δ^{13}C values obtained from the Inche-Rahbari and Khakriz deposits exhibit igneous-derived carbon isotope signature, thus suggesting a magmatic fluid source for the late-stage carbonates (Fig. 14b).

The δ^{18}O values for late-stage hydrothermal carbonate veins range between 3.29‰ to 10.67‰, with an anomalous value of 29.3‰ for one sample. A fluid with this isotopic signature may have magmatic and meteoric fluids sources. This isotopic signature would be similar to the meteoric water in composition consistency which became enriched in δ^{18}O as the result of exchange with fluids from adjacent carbonate rocks. However, most of the values from the carbonate vein indicated a magmatic source, because oxygen isotopic signature ranging from 8 to 9‰ are in the range of normal magmatic waters (Sheppard, 1986).

The δ^{13}C and δ^{18}O values show decreasing trend from the host limestones to the late-stage hydrothermal carbonates (Table 6; Fig. 14b). The carbon and oxygen isotopic compositions of the limestones surrounding the orebody are similar to those of marine carbonates. In contrast, the δ^{13}C and δ^{18}O isotopic ratios from late-stage hydrothermal carbonate may correspond to magmatic values. The decreasing trend of carbon and oxygen isotope compositions from limestones to late-stage hydrothermal carbonate indicates that the fresh limestones were modified due to repeatedly interaction with a hydrothermal fluid with a lower carbon and oxygen isotope ratio (Fig. 14b).

7.3. Skarn and iron mineralization

The global iron skarn deposits are compositionally divided into two types: calcic and magnesian skarns. Calcic skarns are characterized by a mineral sequence with a prograde stage with calcic garnets and pyroxenes followed by a retrograde episode with epidote and actinolite (Einaudi et al., 1981; Purtov et al., 1989); these skarns are mainly associated with dioritic plutons intruded into limestone. In contrast, the magnesian iron skarns mainly consist of a prograde association of forsterite and diopside whereas serpentine and talc are the typical retrograde minerals. Magnesian skarns are common in Cordilleran orogenic belts, and are associated with more silica-rich intrusive rocks than calcic iron skarns including granodiorite, quartz monzonite, and granite (Einaudi et al., 1981).

The KIAG intrusions and associated iron skarn deposits show Cordilleran-type signatures which are different from the island arc setting plutons with calcic skarn deposits. Skarn type iron deposits in the Zanjan district are the result of magmatic fluids related to the emplacement of the Eocene KIAG granodiorite-granite intrusions into the Soltaniyeh dolomite (Precambrian-Cambrian), Mila limestone/dolomite (Cambrian) and Ruteh limestone (Permian) Formations. Calcic skarn formed in limestone at Khakriz, and magnesian skarn in dolomite at Arjin and Inche-Rahbari.

A large amount of magnetite precipitated during the early stages of the retrograde alteration when the temperature of the hydrothermal fluids decreased. The late stages of the retrograde skarn are characterized by the development of sulfide minerals (pyrite, chalcopyrite, bornite and rare galena and sphalerite). In the last stage, calcite and quartz vein and hematite veins cut across magnetite ore, sulfide and calc-silicate minerals.

Iron skarn mineralization in the Zanjan district have many similarities with other Fe skarn deposits common in Cordilleran orogenic belts (Einaudi et al., 1981; Einaudi and Burt, 1982; Zhao et al., 1990; Zürcher et al., 2001; Forster et al., 2004; Meinert et al., 2005): (1) these deposits are associated with granite to granodiorite and quartz-monzonite intrusions, (2) the Khakriz deposit is a calcic skarn and Arjin and Inche-Rahbari deposits are magnesian skarns. The prograde exoskarn zones are rich in garnet, forsterite (except in the Khakriz deposit), pyroxene, and the retrograde units in serpentine and talc (except in the Khakriz deposit), tremolite-actinolite, epidote, chlorite, calcite, and minor amounts of quartz, (3) Iron mineralization replaces limestones of the Ruteh Formations in the Khakriz deposits. But dolomitic rocks of Soltaniyeh and Mila Formations are the main host rocks in the Arjin and Incheh-Rahbari deposits, respectively, (4) magnetite and hematite are the main iron ore minerals and are associated with retrograde mineral assemblages, (5) sulfide minerals such as pyrite, chalcopyrite, bornite, with minor amounts of galena and sphalerite (in the Khakriz deposit) are the main sulfide minerals in these deposits, (6) exoskarn is well developed at these deposits, (7) the distribution of alteration and mineralization during prograde stages was strongly influenced by the composition of the host rocks, (8) magmatic fluids and meteoric water had important role in the mineralization stages.

8. Conclusions

The Zanjan skarn type iron deposit formed due to the intrusion of KIAG suite into carbonate rocks of the Soltaniyeh, Mila and Ruteh Formations. The Khakriz, Inche-Rahbari and Arjin intrusions range in composition from granite to granodiorite and quartz-monzonite. All these Cordilleran-type intrusions show high-potassic calc-alkaline, I-type, and metaluminous characteristics with enrichment in LILE and LREE and depletion in HFSE and HREE. U-Pb zircon dating revealed an age of early Eocene (~53 to 55 Ma) age of emplacement. Geochemical and zircon Hf-O isotopic signatures suggest that the investigated granitoid rocks are the mixture of juvenile mantle-derived melts with partial melts of lower continental crust during the subduction of Neotethyan ocean beneath the Central Iranian terrane.

The Arjin and Inche-Rahbari deposits are classified as magnesian skarns whereas iron mineralization in the Khakriz deposit is a calcic skarn. Ore-forming fluids separated from the KIAG intrusions and replaced the sedimentary carbonate rocks precipitating calc-silicate minerals and magnetite in limestone and dolomite beds. The magnetite precipitated during retrograde skarn formation. Sulfur, oxygen and carbon isotopic signatures are consistent with mineralization formed by the interaction of magmatic hydrothermal fluids with carbonate host rocks.

Acknowledgments

This research was partly funded by the Institute of Geology and Geophysics, Chinese Academy of Sciences (IGGCAS), and by the 2014 SGR 1661 of the Catalan government (the grant number is 201503). Joaquín Perona (Centres Científics i Tecnològics de la Universitat de Barcelona, Catalonia, Spain) performed the stable isotope analyses. We thank Dr. Andreas G. Mueller and an anonymous reviewer for their helpful and constructive comments. All logistical supports during field studies came from the University of Zanjan, Zanjan, Iran.

References

Agard, P., Omrani, J., Jolivet, L., Mouthereau, F., 2005. Convergence history across Zagros (Iran): constraints from collisional and earlier deformation. Int. J. Earth Sci. 94, 401–419.

Agard, P., Omrani, J., Jolivet, L., Whitechurch, H., Vrielynck, B., Spakman, W., Moni, E.P., Meyer, B., Wortel, R., 2011. Zagros orogeny: a subduction-dominated process. Geol. Mag. 148, 692–725.

Alavi, M., 1994. Tectonics of the Zagros orogenic belt of Iran: new data and interpretations. Tectonophysics 229, 211–238.

Alavi, M., 2004. Regional stratigraphy of the Zagros fold-thrust belt of Iran and its proforeland evolution. Am. J. Sci. 304, 1–20.

Alavi, M., 2007. Structures of the Zagros fold-thrust belt in Iran. Am. J. Sci. 307, 1064–1095.

Amelin, Y., Lee, D.C., Halliday, A.N., Pidgeon, R.T., 1999. Nature of the Earth's earliest crust from hafnium isotopes in single detrital zircons. Nature 399, 252–255.

Asiabanha, A., Foden, J., 2012. Post-collisional transition from an extensional volcano-sedimentary basin to a continental arc in the Alborz Ranges, N-Iran. Lithos 148, 98–111.

Balaghi Einalou, M., Sadeghian, M., Minggou, Z., Ghasemi, H., Mohajjel, M., 2014. Zircon U-Pb ages, Hf isotopes and geochemistry of the schists, gneisses and granites in Delbar metamorphic-igneous complex, SE of Shahrood (Iran): implications for Neoproterozoic geodynamic evolutions of Central Iran. J. Asian Earth Sci. 92, 92–124.

Ballato, P., Mulch, A., Landgraf, A., Strecker, M.R., Dalconi, M.C., Friedrich, A., Tabatabaei, S.H., 2011. Middle to late Miocene Middle Eastern climate from stable oxygen and carbon isotope data, southern Alborz mountains, N. Iran. Earth Planet. Sci. Lett. 300, 125–138.

Be′ eri-Shlevin, Y., Katzir, Y., Blichert-Toft, J., Kleinhanns, I.C., Whitehouse, M., 2010. Nd-Sr-Hf-O isotope provinciality in northernmost Arabian-Nubian Shield: implication for crustal evolution. Contrib. Mineral. Petrol. 160, 181–201.

Belousova, E.A., Griffin, W.L., O'Reilly, S.Y., 2006. Zircon crystal morphology, trace element signatures and Hf isotope composition as a tool for petrogenetic modelling: examples from eastern Australian granitoids. J. Petrol. 47, 329–353.

Belousova, E., Kostitsyn, Y.A., Griffin, W.L., Begg, G.C., O'Reilly, S.Y., Pearson, N.J., 2010. The growth of the continental crust: constraints from zircon Hf-isotope data. Lithos 119, 457–466.

Berberian, F., Berberian, M., 1981. Tectono-plutonic episodes in Iran. In: Gupta, H.K., Delany, F.M. (Eds.), Zagros, Hindu Kush, Himalaya Geodynamic Evolution 3. American Geophysical Union, Washington, D.C., pp. 5–32.

Berberian, M., King, G.C.P., 1981. Towards a paleogeography and tectonic evolution of Iran. Can. J. Earth Sci. 18, 210–265.

Blichert-Toft, J., Albarède, F., 1997. The Lu-Hf geochemistry of chondrites and the evolution of the mantle-crust system. Earth Planet. Sci. Lett. 148, 243–258.

Bowman, J.R., 1998. Stable isotope systematic of skarns. In: Lentz, D.R. (Ed.), Mineralized Intrusion-related Skarn Systems. Min. Assoc. Canada Short Course Series 26, pp. 99–145.

Chappell, B.W., White, A.J.R., 2001. Two contrasting granite types. 25 years later. Aust. J. Earth Sci. 48, 489–499.

Chen, Y.J., Ni, P., Fan, H.R., Pirajno, F., Lai, Y., Su, W.C., Zhang, H., 2007. Diagnostic fluid inclusions of different types of hydrothermal gold deposits. Acta Petrol. Sin. 23, 2085–2108.

Chiu, H.Y., Chung, S.L., Zarrinkoub, M.H., Mohammadi, S.S., Khatib, M.M., Iizuka, Y., 2013. Zircon U-Pb age constraints from Iran on the magmatic evolution related to Neotethyan subduction and Zagros orogeny. Lithos 162–163, 70–87.

Collins, W.J., Beams, S.D., White, A.J.R., Chappell, B.W., 1982. Nature and origin of A-type granites with particular reference to southeastern Australia. Contrib. Mineral. Petrol. 80, 189–200.

Daliran, F., 2002. Kiruna-type iron oxide-apatite ores and apatitites of the Bafq district, Iran, with an emphasis on the REE geochemistry of their apatites. In: Porter, T.M. (Ed.), Hydrothermal Iron Oxide Copper Gold and Related Deposits. A Global Perspective v. 2. PGC Publishing, Adelaide, pp. 303–320.

Daliran, F., Stosch, H.G., Williams, P., 2007. Multistage metasomatism and mineralization at hydrothermal Fe oxide-REE-apatite deposits and 'apatitites' of the Bafq district, central-east Iran. In: Stanely, C.J. (Ed.), Digging Deeper, Proceedings 9th Biennial SGA Meeting Dublin, Ireland, pp. 1501–1504.

Daliran, F., Stosch, H.G., Williams, P., Jamli, H., Dorri, M.B., 2010. Early Cambrian Iron Oxide-Apatite-REE (U) Deposits of the Bafq District, East-Central Iran. In: Corriveau, L., Mumin, H. (Eds.), Exploring for Iron oxide copper-gold deposits: Canada and Global analogues 20. Geol Assoc Canada, Short Course Notes, pp. 143–155.

De la Roche, H., Leterrier, J., Grande Claude, P., Marchal, M., 1980. A classification of volcanic and plutonic rocks using R1-R2 diagrams and major element analyses, its relationships and current nomenclature. Chem. Geol. 29, 183–210.

Einaudi, M.T., Burt, D.M., 1982. A special issue devoted to skarn deposits-introduction, terminology, classification and composition of skarn deposits. Econ. Geol. 77, 745–754.

Einaudi, M.T., Meinert, L.D., Newberry, R.J., 1981. Skarn deposits. Econ. Geol. 75th Anniversary Volume, pp. 317–391.

Forster, D.B., Seccombe, P.K., Philips, D., 2004. Controls on skarn mineralization and alteration at the Cadia deposits, New South Wales, Australia. Econ. Geol. 99, 761–788.

Foster, H., Jafarzadeh, A., 1994. The Bafq mining district in Central Iran-a highly mineralized Infracambrian volcanic field. Econ. Geol. 89, 1697–1721.

Frost, B.R., Barnes, C.G., Collins, W.J., Arculus, S.R.J., Ellis, D.J., Frost, C.D., 2001. A geochemical classification for granitic rocks. J. Petrol. 42, 2033–2048.

Ganino, C., Arndt, N.T., Zhou, M.F., Gaillard, F., Chauvel, C., 2008. Interaction of magma with sedimentary wall rock and magnetite ore genesis in the Panzhihua mafic intrusion, SW China. Mineral. Deposita 43, 677–694.

Golmohammadi, A., Karimpour, M.H., Malekzadeh Shafaroudi, A., Mazaheri, S.A., 2014. Alteration-mineralization, and radiometric ages of the source pluton at the Sangan iron skarn deposit, northeastern Iran. Ore Geol. Rev. 65, 545–563.

Goodge, J.W., Vervoort, J.D., 2006. Origin of Mesoproterozoic A-type granites in Laurentia: Hf isotope evidence. Earth Planet. Sci. Lett. 243, 711–731.

Griffin, W.L., Pearson, N.J., Belousova, E.A., Saeed, A., 2006. Comment: Hf-isotope heterogeneity in zircon 91500. Chem. Geol. 233, 358–363.

Griffin, W.L., Wang, X., Jackson, S.E., Pearson, N.J., O'Reilly, S.Y., Xu, X., Zhou, X., 2002. Zircon chemistry and magma mixing, SE China: in-situ analysis of Hf isotopes, Tonglu and Pingtan igneous complexes. Lithos 61 (3–4), 237–269.

Hildreth, W., 1981. Gradients in silicic magma chambers-implications for lithospheric magmatism. J. Geophys. Res. 86, 153–192.

Honarmand, M., Rashidnejad Omran, N., Neubauer, N., Emami, M.H., Nabatian, G., Liu, X., Donge, Y., von Quadt, A., Chen, B., 2014. Laser-ICP-MS U-Pb zircon ages and geochemical and Sr-Nd-Pb isotopic compositions of the Niyasar plutonic complex, Iran: constraints on petrogenesis and tectonic evolution. Int. Geol. Rev. 56, 104–132.

Horton, B.K., Hassanzadeh, J., Stockli, D.F., Axen, G.J., Gillis, R.J., Guest, B., Amini, A., Fakhari, M.D., Zamanzadeh, S.M., Grove, M., 2008. Detrital zircon provenance of Neoproterozoic to Cenozoicdeposits in Iran: implications for chronostratigraphy and collisional tectonics. Tectonophysics 451, 97–122.

Jafari, S.M., Shemirani, A., Hamdi, B., 2007. Microstratigraphy of the Late Ediacaran to the Ordovician in NW Iran (Takab area). In: Vickers-Rich, P., Komarower, P. (Eds.), The Rise and Fall of the Ediacaran Biota 286. Geological Society of London Special Publication, pp. 433–437.

Jami, M., Dunlop, A.C., Cohen, D.R., 2007. Fluid inclusion and stable isotope study of the Esfordi apatite-magnetite deposit, Central Iran. Econ. Geol. 102, 1111–1128.

Jamtveit, B., Andersen, T., 1993. Contact metamorphism of layered shale-carbonate sequences in the Oslo Rift; III, the nature of skarn-forming fluids. Econ. Geol. 88, 1830–1849.

Kargaranbafghi, F., Foeken, J., Guest, B., Stuart, F., 2012. Cooling history of the Chapedony metamorphic core complex, Central Iran: Implications for the Eurasia-Arabia collision. Tectonophysics 524–525, 100–107.

Karimpour, M.H., 1989. Applied Economic Geology. Javid Publication, Mashhad, Iran (404 pp.).

Karimzadeh Somarin, A., Moayyed, M., 2002. Granite- and gabbro-diorite-associated skarn deposits of NW Iran. Ore Geol. Rev. 20, 127–138.

Kemp, A.I.S., Hawkesworth, C.J., Collins, W.J., Gray, C.M., Blevin, P.L., Eimf, 2009. Isotopic evidence for rapid continental growth in an extensional accretionary orogen: the Tasmanides, eastern Australia. Earth Planet. Sci. Lett. 284, 455–466.

Kunzmann, T., 1999. The aenigmatite-rhodonite mineral group. Eur. J. Mineral. 11, 743–756.

Lenting, C., Geisler, T., Gerdes, A., Koolman, E., Scherer, E., Zeh, A., 2010. The behavior of the Hf isotope system in radiation-damaged zircon during experimental hydrothermal alteration. Am. Mineral. 95, 1343–1348.

Li, X.H., Li, W.X., Wang, X.C., Li, Q.L., Liu, Y., Tang, G.Q., 2009a. Role of mantle-derived magma in genesis of early Yanshanian granites in the Nanling Range, South China: in situ zircon Hf-O isotopic constraints. Sci. China Ser. D Earth Sci. 52, 1262–1278.

Li, X.H., Liu, Y., Li, Q.L., Guo, C.H., Chamberlain, K.R., 2009b. Precise determination of Phanerozoic zircon Pb/Pb age by multi-collector SIMS without external standardization. Geochem. Geophys. Geosyst. 10, Q04010. http://dx.doi.org/10.1029/2009GC002400.

Li, X.-H., Li, Z.-X., Li, W.-X., Liu, Y., Yuan, C., Wei, G., Qi, C., 2007. U-Pb zircon, geochemical and Sr-Nd-Hf isotopic constraints on age and origin of Jurassic I-and A-type granites from central Guangdong, SE China: a major igneous event in response to foundering of a subducted flat-slab? Lithos 96, 186–204.

Li, Q.L., Li, X.H., Liu, Y., Tang, G.Q., Yang, J.H., Zhu, W.G., 2010a. Precise U-Pb and Pb-Pb dating of Phanerozoic baddeleyite by SIMS with oxygen flooding technique. J. Anal. At. Spectrom. 25, 1107–1113.

Li, X.H., Long, W.G., Li, Q.L., Liu, Y., Zheng, Y.F., Yang, Y.H., Chamberlain, K.R., Wan, D.F., Guo, C.H., Wang, X.C., Tao, H., 2010b. Penglai zircon megacrysts: a potential new working reference material for microbeam determination of Hf-O isotopes and U-Pb age. Geostand. Geoanal. Res. 34 (2), 117–134.

Li, X.H., Tang, G.Q., Gong, B., Yang, Y.H., Hou, K.J., Hu, Z.C., Li, Q.L., Liu, Y., Li, W.X., 2013. Qinghu zircon: a working reference for microbeam analysis of U-Pb age and Hf and O isotopes. Chin. Sci. Bull. 58.

Ludwig, K.R., 2003. User's Manual for Isoplot 3.00: A Geochronological Toolkit for Microsoft Excel. 4. Special Publication/Berkeley Geochronology Center, p. 74.

Maanijou, M., 2002. Proterozoic metallogeny of Iran. International Symposium of Metallogeny of Precambrian Shields, p. 2.13 (Kyiv, Ukraine).

Maniar, P.D., Piccoli, P.M., 1989. Tectonic discrimination of granitoids. Geol. Soc. Am. Bull. 101, 635–643.

Mazaheri, S.A., Andrew, A.S., Chenhall, B.E., 1994. Petrological studies of Sangan iron ore deposit. Center for isotope studies, Research Report, Sydney, Australia, pp. 48–52.

McCrea, J.M., 1950. On the isotopic chemistry of carbonates and a paleotemperature scale. J. Chem. Phys. 18, 849–857.

McDonough, W.F., Sun, S.S., 1995. Composition of the Earth. Chem. Geol. 120, 223–253.

Meinert, L.D., 1983. Variability of skarn deposits: guides to exploration. In: Boardman, S.J. (Ed.), Revolution in the Earth Sciences. Kendall-Hunt Publishing Company, Iowa, pp. 301–316.

Meinert, L.D., 1992. Skarns and skarn deposits. Geosci. Can. 19, 145–162.

Meinert, L.D., Dipple, G., Nicolescu, S., 2005. World skarn deposits. Econ. Geol. 100th Anniv. 299–336.

Meinert, L.D., Lentz, D.R., Newberry, R.J., 2000. A special issue devoted to skarn deposits. Econ. Geol. 95 (6), 1183–1365.

Mohajjel, M., Fergusson, C.L., 2000. Dextral transpression in Late Cretaceous continental collision Sanandaj-Sirjan zone western Iran. J. Struct. Geol. 22, 1125–1139.

Mueller, A.M., 1991. The Savage Lode magnesian skarn in the Marvel Loch gold–silver mine, Southern Cross greenstone belt, Western Australia. Part 1: structural setting, petrography, and geochemistry. Can. J. Earth Sci. 28 (5), 659–685.

Mueller, A.M., Groves, D.I., Delor, C.P., 1991. The Savage Lode magnesian skarn in the Marvel Loch gold-silver mine, Southern Cross greenstone belt, Western Australia. Part 2: pressure-temperature estimates and constraints on fluid sources. Can. J. Earth Sci. 28 (5), 686–705.

Nabatian, G., Ghaderi, M., Neubauer, F., Honarmand, M., Lui, X., Dong, Y., Jiang, S.Y., Bernroider, M., 2014. Petrogenesis of Tarom high-potassic granitoids in the Alborz-Azarbaijan belt, Iran: Geochemical, U-Pb zircon and Sr-Nd-Pb isotopic constraints. Lithos 184–187, 324–345.

Nabatian, G., Rastad, E., Neubauer, F., Honarmand, M., Ghaderi, M., 2015. Iron and Fe-Mn mineralisation in Iran: implications for Tethyan metallogeny. Aust. J. Earth Sci. 62, 211–241.

Nasdala, L., Hofmeister, W., Norberg, N., Mattinson, J.M., Corfu, F., Dörr, W., Kamo, S.L., Kennedy, A.K., Kronz, A., Reiners, P.W., Frei, D., Kosler, J., Wan, Y., Götze, J., Häger, T., Kröner, A., Valley, J.W., 2008. Zircon M257-a homogeneous natural reference material for the ion microprobe U-Pb analysis of zircon. Geostand. Geoanal. Res. 32, 47–265.

Nutman, A.P., Mohajjel, M., Bennett, V.C., Fergusson, C.L., 2014. Gondwanan Eoarchean-Neoproterozoic ancient crustal material in Iran and Turkey: zircon U-Pb-Hf isotopic evidence. Can. J. Earth Sci. 51 (3), 272–285.

O′ Neill, J.M., Klein, T.L., Sims, P.K., 2002. Metallogeny of a Palaeoproterozoic Collisional Orogen Through Time-The Great Falls Tectonic Zone, Montana and Idaho. 34. Geological Society of America, p. 336 Abstracts with Programs.

Ohmoto, H., 1972. Systematics of sulfur and carbon isotopes in hydrothermal ore deposits. Econ. Geol. 67, 551–577.

Ohmoto, H., Rye, R.O., 1979. Isotopes of sulfur and carbon. In: Barnes, H.L. (Ed.), Geochemistry of Hydrothermal Ore Deposits (II). John Wiley and Sons, New York, pp. 509–567.

Pan, Y., Dong, P., 1999. The Lower Changjiang (Yangzi/Yangtze River) metallogenic belt, east central China: intrusion- and wall rock-hosted Cu-Fe-Au, Mo, Zn, Pb, Ag deposits. Ore Geol. Rev. 15, 177–242.

Pirajno, F., 2009. Hydrothermal Processes and Mineral Systems. Springer, Berlin, pp. 1–1250.

Purtov, V.K., Kholodnoc, V.V., Anfilogov, V.N., Nechkin, G.S., 1989. The role of chlorine in the formation of magnetite skarn. Int. Geol. Rev. 31, 63–71.

Ray, J.S., Ramesha, R., Pandea, K., Trivedi, J.R., Shukla, P.N., Patel, P.P., 2000. Isotope and rare earth element chemistry of carbonatite ± alkaline complexes of Deccan volcanic province: implications to magmatic and alteration processes. J. Asian Earth Sci. 18, 177–194.

Ren, T., Zhang, X., Runsheng Han, R., Hou, B., 2015. Carbon-oxygen isotopic covariations of calcite from Langdu skarn copper deposit, China: implications for sulfide precipitation. Chin. J. Geochem. 34 (1), 21–27.

Romer, R., Soler, A., 1995. U-Pb age and lead isotopic characterization of Au-bearing skarn related to the Andorra granite (central Pyrenees, Spain). Mineral. Deposita 30, 374–383.

Rose, A.W., Herrick, D.C., Deines, P., 1985. An oxygen and sulfur isotope study of skarn type magnetite deposits of the Cornwall type, Southeastern Pennsylvania. Econ. Geol. 80, 418–443.

Scherer, E.E., Münker, C., Mezger, K., 2001. Calibration of the lutetium-hafnium clock. Science 293, 683–687.

Seal II, R.R., 2006. Sulfur isotope geochemistry of sulfide minerals. Rev. Mineral. Geochem. 61, 633–677.

Sengör, A.M.C., Altiner, D., Cin, A., Ustaömer, T., HsϋK, J., 1988. The origin and assembly of the Tethyside orogenic collage at the expense of Gondwana land. In: Audley-Charles, M.G., Hallam, A. (Eds.), Gondwana and Tethys 37. Geological Society [London] Special Publication, (London UK), pp. 119–181.

Shafaii Moghadam, H., Li, X.-H., Stern, R.J., Santos, J.F., Ghorbani, G., Pourmohsen, M., 2016. Age and nature of 560-520 Ma calc-alkaline granitoids of Biarjmand, northeast Iran: insights into Cadomian arc magmatism in northern Gondwana. Int. Geol. Rev. 58 (12), 1492–1509.

Shen, J.F., Santosh, M., Li, S.R., Zhang, H.F., 2013. The Beiminghe skarn iron deposit, eastern China: geochronology, isotope geochemistry and implications for the destruction of the North China Craton. Lithos 156–159, 218–229.

Sheppard, S.M.F., 1986. Igneous rocks: III. Isotopic case studies of magmatism in Africa, Eurasia and oceanic islands. In: Valley, J.W., Taylor, H.P., O′ Neil, J.R. (Eds.), Stable Isotopes in High Temperature Geological ProcessesM.S.A. Rev. Mineral 16. Mineralogical Society of America, Washington, pp. 319–371.

Shimazaki, H., Shimizu, M., Nakano, T., 1986. Carbon and oxygen isotopes of calcites from Japanese skarn deposits. Geochem. J. 20, 297–310.

Sláma, J., Košler, J., Condon, D.J., Crowley, J.L., Gerdes, A., Hanchar, J.M., Horstwood, M.S.A., Morris, G.A., Nasdala, L., Norberg, N., Schaltegger, U., Schoene, B., Tubrett, M.N., Whitehouse, M.J., 2008. Plešovice zircon-a new natural reference material for U-Pb and Hf isotopic microanalysis. Chem. Geol. 249, 1–35.

Spiro, B., Puig, A., 1988. The source of sulphur in polymetallic deposits in the Cretaceous magmatic arc, Chilean Andes. J. S. Am. Earth Sci. 1, 261–266.

Stacey, J.S., Kramers, J.D., 1975. Approximation of terrestrial lead isotope evolution by a 2-stage model. Earth Planet. Sci. Lett. 26, 207–221.

Stocklin, J., Eftekharnezhad, J., 1969. Geological Map of Zanjan 1:250,000, 1 Sheet. Geological Survey of Iran, Tehran Iran.

Stocklin, J., Ruttner, A., Nabavi, M., 1964. New data on the lower Paleozoic, North Iran. Geological Survey of Iran, Report, p. 1.

Tang, G.Q., Li, X.H., Li, Q.L., Liu, Y., Ling, X.X., Yin, Q.Z., 2015. Deciphering the physical mechanism of the topography effect for oxygen isotope measurements using a Cameca IMS-1280 SIMS. J. Anal. At. Spectrom. 30, 950–956.

Taylor, B.E., 1986. Magmatic volatiles: isotopic variation of C, H, and S. M.S.A. Rev. Mineral. 16, 185–226.

Valley, J.W., 2003. Oxygen isotopes in zircons. Rev. Mineral. Geochem. 53, 343–385.

Valley, J.W., Kinny, P.D., Schulze, D.J., Spicuzza, M.J., 1998. Zircon megacrysts from Kimberlite: oxygen isotope variability among mantle melts. Contrib. Mineral. Petrol. 133, 1–11.

Valley, J.W., Lackey, J.S., Cavosie, A.J., Clechenko, C.C., Spicuzza, M.J., Basei, M.A.S., Bindeman, I.N., Ferreira, V.P., Sial, A.N., King, E.M., Peck, W.H., Sinha, A.K., Wie, C.S., 2005. 4.4 billion years of crustal maturation: oxygen isotope ratios of magmatic zircon. Contrib. Mineral. Petrol. 150, 561–580.

Veizer, J., Holser, W.T., Wilgus, C.K., 1980. Correlation of $^{13}C/^{12}C$ and $^{34}S/^{32}S$ secular variations. Geochim. Cosmochim. Acta 44, 579–587.

Verdel, C., Wernicke, B.P., Hassanzadeh, J., Guest, B., 2011. A Paleogene extensional arc flare-up in Iran. Tectonics 30:TC3008. http://dx.doi.org/10.1029/2010TC002809.

Verdel, C., Wernicke, B.P., Ramezani, J., Hassanzadeh, J., Renne, P.R., Spell, T.L., 2007. Geology and thermochronology of Tertiary Cordilleran-style metamorphic core complexes in the Saghand region of central Iran. Geol. Soc. Am. Bull. 119, 961–977.

Vervoort, J.D., Blichert-Toft, J., 1999. Evolution of the depleted mantle: Hf isotope evidence from juvenile rocks through time. Geochim. Cosmochim. Acta 63, 533–556.

Vincent, S.J., Allen, M.B., Ismail-Zadeh, A.D., Flecker, R., Foland, K.A., Simmons, M.D., 2005. Insights from the Talysh of Azerbaijan into the Paleogene evolution of the South Caspian region. Geol. Soc. Am. Bull. 117, 1513–1533.

Wan, B., Zhang, L.C., Xiao, W.J., 2010. Geological and geochemical characteristics and ore genesis of the Keketale VMS Pb-Zn deposit, Southern Altay Metallogenic Belt, NW China. Ore Geol. Rev. 37, 114–126.

Wu, F.Y., Yang, Y.H., Xie, L.W., Yang, J.H., Xu, P., 2006. Hf isotopic compositions of the standard zircons and baddeleyites used in U-Pb geochronology. Chem. Geol. 234 (1–2), 105–126.

Xie, G.Q., Mao, J.W., Zhu, Q.Q., Yao, L., Li, Y.H., Li, W., Zhao, H.J., 2015. Geochemical constraints on Cu-Fe and Fe skarn deposits in the Edong district, Middle-Lower Yangtze River metallogenic belt, China. Ore Geol. Rev. 64, 425–444.

Zhao, Y., Lin, W., Bi, C., Li, D., 1990. Skarn deposits in China. Beijing Geological Publishing House, China (354 pp.).

Zheng, Y., 2001. Theoretical modeling of stable isotope systems and its applications to geochemistry of hydrothermal ore deposits. J. Miner. Depos. 20, 56–71 (in Chinese with English abstract).

Zheng, J.P., Griffin, W.L., O'Reilly, S.Y., Zhang, M., Pearson, N.J., Pan, Y.M., 2006. Widespread Archean basement beneath the Yangtze Craton. Geology 34, 417–420.

Zürcher, L., Ruíz, J., Barton, M., 2001. Paragenesis, elemental distribution, and stable isotopes at the Peña Colorada iron skarn, Colima, Mexico. Econ. Geol. 96, 535–557.